PHYSICAL REVIEW A **106**, 012601 (2022)

Quantum-enhanced passive remote sensing

Emre Köse,[1,*] Gerardo Adesso,[2,†] and Daniel Braun[1,‡]
[1]*Institut für Theoretische Physik, Eberhard Karls Universität Tübingen, 72076 Tübingen, Germany*
[2]*School of Mathematical Sciences, University of Nottingham, University Park, Nottingham NG7 2RD, United Kingdom*

(Received 23 December 2021; accepted 6 June 2022; published 6 July 2022)

We investigate theoretically the ultimate resolution that can be achieved with passive remote sensing in the microwave regime used, e.g., on board of satellites observing Earth, such as the soil moisture and ocean salinity (SMOS) mission. We give a fully quantum mechanical analysis of the problem, starting from thermal distributions of microscopic currents on the surface to be imaged that lead to a mixture of coherent states of the electromagnetic field which are then measured with an array of antennas. We derive the optimal detection modes and measurement schemes that allow one to saturate the quantum Cramér-Rao bound for the chosen parameters that determine the distribution of the microscopic currents. For parameters comparable to those of SMOS, a quantum enhancement of the spatial resolution by more than a factor of 20 should be possible with a single measurement and a single detector, and a resolution down to the order of 1 m and less than a $\frac{1}{10}$ K for the theoretically possible maximum number of measurements.

DOI: 10.1103/PhysRevA.106.012601

I. INTRODUCTION

Optical imaging has evolved dramatically since the discovery that Abbe's and Rayleigh's resolution limit comparable to the wavelength of the used light is not a fundamental bound. This was demonstrated experimentally with a series of works starting with stimulated emission depletion in 1994 by Hell [1], who showed that decorating molecules with fluorophores and quenching these selectively, imaging of a molecule with nanometer resolution could be achieved in the optical domain (see [2] for a review). This was followed in 2016 by theoretical work by Tsang and coworkers [3] who framed the problem of the ultimate resolution of two-point sources in terms of quantum parameter estimation, a very natural approach given that quantum parameter estimation theory was originally motivated by generalizing the classical Cramér-Rao bound that had long been used in radar detection to the optical domain [4–7]. Tsang and coworkers showed that even in the limit of vanishing spatial separation between the two sources a finite quantum Fisher information (QFI) for that parameter remains, whereas the classical Fisher information degrades in agreement with Rayleigh's bound [8]. A large body of theoretical work followed that incorporated important concepts such as the point spread function for analyzing optical lens systems, and mode engineering such as SPADE for optimal detection modes [8–25], reminiscent of the engineering of a "detector mode" for single-parameter estimation of light sources [26]. Experimental work in recent years validated this new approach to imaging [27–30]. Optical interferometers were investigated in [21,31–33]. The resolution for general parameter estimation for weak thermal sources was studied in [34]. Recently, the spatial resolution of two point sources for two-mode interferometers was examined for the far-field regime [35].

In this work, we investigate the ultimate limits of passive remote sensing in the microwave regime with a satellite of the surface of Earth. There, the state of the art is the use of antenna arrays for synthesizing interferometrically a large antenna with corresponding enhanced resolution. For example, the SMOS (soil moisture and ocean salinity) interferometer achieves a resolution of about 35 km, flying at the height of about 758 km and using a Y-shaped array of 69 antenna [36–39]. Each antenna measures in a narrow frequency band 1420–1427 MHz with a central wavelength around $\lambda \sim 21$ cm and in real time the electric fields corresponding to the thermal noise emitted by Earth according to the local brightness temperatures on its surface. The signals are filtered and interfered numerically, implementing thus purely classical interference, which implies a resolution governed by the van Cittert–Zernike theorem [40–42]. Recently, it was shown theoretically that larger baselines can be synthesized by using the motion of the satellite but at the price of the radiometric (i.e., temperature) resolution [43]. The question naturally arises to what extent the resolution can be improved by using methods of quantum metrology. As in the optical domain the answer can be found by analyzing the quantum Cramér-Rao bound and then trying to find the optimal measurements that can achieve it. We solve this problem, in general, for an arbitrary antenna array defined by the positions of individual antenna, in the sense of finding, at least numerically, the optimal modes for measuring the electric fields. We go beyond the situation of localized point sources that has become a favorite simplification in the field and describe the sources as randomly fluctuating microscopic current distributions which in turn generate the electromagnetic field noise, ultimately measured by the

---

[*] saban-emre.koese@uni-tuebingen.de
[†] gerardo.adesso@nottingham.ac.uk
[‡] daniel.braun@uni-tuebingen.de

satellite. This is closer to the literature on passive remote sensing in the microwave regime and allows a direct comparison with the van Cittert–Zernike theorem. We also make use of the scattering matrix formalism introduced in this context in [44]. The thermal fluctuations of the microscopic currents lead to Gaussian states of the microwave field [26,45–47], and our analysis makes therefore heavy use of the quantum Cramér-Rao bound (QCRB) for Gaussian states [48–53]. We assume that only the current densities at the surface of Earth contribute. In reality, the emission seen by the SMOS is from a surface layer on Earth that has a finite thickness, but is thin enough to make a two-dimensional (2D) approximation. Also, the receivers see the emission from the cosmic microwave background. We neglect it as its temperature is two orders of magnitude lower than the one of Earth [43]. Additional technical noises are neglected and indeed beyond the scope of this paper. Additional technical noises in the context of imaging were considered in Refs. [54–56].

The rest of the paper is organized as follows. In Sec. II, we describe the state for the n-mode interferometer for general sources on the source plane using the scattering matrix formalism. Later, we present the general formula of the positive-operator-valued measure (POVM) for the QFI based on the state of the n-mode interferometer. In Sec. III, first, we discuss the QFI for the parameters, source size, and temperature of a single uniform circular source for both a single antenna and two antennas. Second, we discuss the spatial resolution, source separation, and centroid on the source plane, of two strong point sources with the same and different temperatures for a two-mode interferometer. Third, we examine an array of antennas to increase the spatial resolution of a uniform circular source and two-point sources. We conclude in Sec. IV.

II. THEORY

A. Continuous vector potential and interaction with classical current sources

The operators for the quantized vector potential $\mathbf{A}(\mathbf{r},t)$ can be written in continuous form. The operator for the vector potential in the Coulomb gauge reads as [57,58]

$$\hat{\mathbf{A}}(\mathbf{r},t) = \int d^3k \left(\frac{\hbar}{16\pi^3\varepsilon_0 c|\mathbf{k}|}\right)^{1/2} \times \sum_{\sigma=1,2} \boldsymbol{\varepsilon}(\mathbf{k},\sigma)\hat{a}(\mathbf{k},\sigma)\exp(-ic|\mathbf{k}|t + i\mathbf{k}\cdot\mathbf{r}) + \text{H.c.}, \tag{1}$$

where, $\hat{a}(\mathbf{k},\sigma)$ are the continuous mode operators with $[\hat{a}(\mathbf{k},\sigma),\hat{a}^\dagger(\mathbf{k},\sigma)] = \delta(\mathbf{k}-\mathbf{k}')\delta_{\sigma\sigma'}$, and $\boldsymbol{\varepsilon}(\mathbf{k},\sigma)$ are the directions of the polarizations with index $\sigma \in 1, 2$, which are always perpendicular to wave vector $\mathbf{k}$. Mode functions are plane waves and parametrized by $\mathbf{k}$ and σ. The interaction Hamiltonian for the classical current distribution of the sources $\mathbf{j}(\mathbf{r},t)$ with electromagnetic waves in free space is given by [43,58–60]

$$H_I(t) = -\int d^3r\, \mathbf{j}(\mathbf{r},t)\cdot\hat{\mathbf{A}}(\mathbf{r},t). \tag{2}$$

In the interaction picture, using the Schrödinger equation the state of the electromagnetic field at time t can be obtained from the one at t_0 as [58–61]

$$|\psi(t)\rangle = U(t,t_0)|\psi(t_0)\rangle, \tag{3}$$

where the $U(t,t_0)$ is given by

$$U(t,t_0) = \exp\left(\frac{i}{\hbar}\int_{t_0}^{t} dt' \int d^3r\, \mathbf{j}(\mathbf{r},t')\cdot\hat{\mathbf{A}}(\mathbf{r},t') + i\varphi(t,t_0)\right). \tag{4}$$

The phase $\varphi(t,t_0)$ is a real number, which arises from the classical interaction between the currents. It is independent of the state on which the propagator acts, and cancels in the calculation of equal-time matrix elements. Since the current density commutes with the vector potential, one can write the time evolution in the form of a displacement operator, which is given by

$$D(\{\alpha(\mathbf{k},\sigma)\}) = \exp\left[\sum_\sigma \int d^3k\, [\alpha(\mathbf{k},\sigma)\hat{a}^\dagger(\mathbf{k},\sigma) - \alpha^*(\mathbf{k},\sigma)\hat{a}(\mathbf{k},\sigma)]\right], \tag{5}$$

where $\alpha(\mathbf{k},\sigma)$ can be found as

$$\alpha(\mathbf{k},\sigma) = \frac{i}{\hbar}\left(\frac{\hbar}{16\pi^3\varepsilon_0 c|\mathbf{k}|}\right)^{1/2} \int_{t_0}^{t} dt' \int d^3r\, \mathbf{j}(\mathbf{r},t')\cdot\boldsymbol{\varepsilon}(\mathbf{k},\sigma) \times \exp(ic|\mathbf{k}|t' - i\mathbf{k}\cdot\mathbf{r}). \tag{6}$$

The $\alpha(\mathbf{k},\sigma)$ also depends on t and t_0. We assume that for $t_0 \to -\infty$ we have the vacuum state $|\{0\}\rangle$ for all modes. For a deterministic current density, $|\psi(t)\rangle$ is a tensor product of coherent states,

$$|\psi(t)\rangle = |\{\alpha(\mathbf{k},\sigma)\}\rangle = D[\{\alpha(\mathbf{k},\sigma)\}]|\{0\}\rangle. \tag{7}$$

One can introduce the Fourier transform (FT) of the current densities and take the t' integral immediately [43]. We introduce the Fourier decomposition of current density as

$$\mathbf{j}(\mathbf{r},t') = \frac{1}{\sqrt{2\pi}}\int_{-\infty}^{\infty} d\tilde{\omega}\, \tilde{\mathbf{j}}(\mathbf{r},\tilde{\omega})\exp(i\tilde{\omega}t'). \tag{8}$$

Then we can write $\alpha(\mathbf{k},\sigma)$ in the form

$$\alpha(\mathbf{k},\sigma) = \frac{i}{\hbar}\left(\frac{\hbar}{32\pi^4\varepsilon_0 c|\mathbf{k}|}\right)^{1/2} \times \int_{-\infty}^{t} dt' \int d^3r \int_{-\infty}^{\infty} d\tilde{\omega}\, \tilde{\mathbf{j}}(\mathbf{r}',\tilde{\omega})\cdot\boldsymbol{\varepsilon}(\mathbf{k},\sigma) \times \exp(ic|\mathbf{k}|t' - i\mathbf{k}\cdot\mathbf{r})\exp(i\tilde{\omega}t'). \tag{9}$$

Taking the integral over t' gives

$$\alpha(\mathbf{k},\sigma) = -\left(\frac{1}{32\pi^4\varepsilon_0 c\hbar|\mathbf{k}|}\right)^{1/2} \times \int d^3r \int_{-\infty}^{\infty} d\tilde{\omega}\, \tilde{\mathbf{j}}(\mathbf{r},\tilde{\omega})\cdot\boldsymbol{\varepsilon}(\mathbf{k},\sigma)\exp(-i\mathbf{k}\cdot\mathbf{r}) \times \frac{\exp[i(\tilde{\omega}+c|\mathbf{k}|)t]}{i\epsilon - c|\mathbf{k}| - \tilde{\omega}}. \tag{10}$$

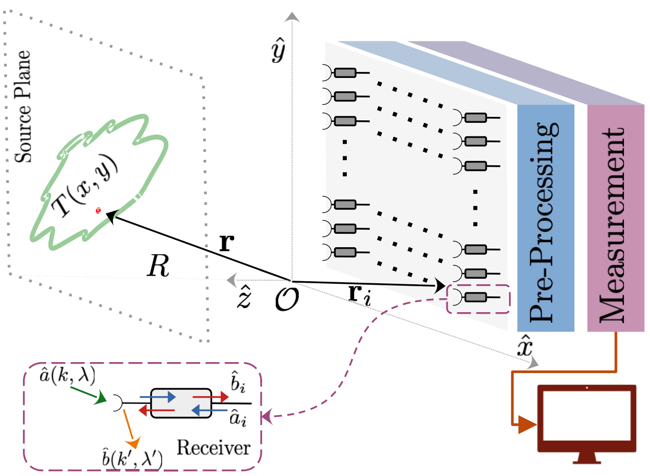

FIG. 1. An interferometer, with n antennas, separated by a distance R from the source plane. The $T_{\text{eff}}(x,y)$ is the position-dependent effective temperature in the source plane that one wants to measure. The field $\hat{a}(\mathbf{k},\sigma)$ propagating from the source enters the receiver on the interferometer and is partly reflected back into the modes $\hat{b}(\mathbf{k},\sigma)$. Single $\hat{b}_i$ exit the receiver and are combined in a preprocessing step, while other single modes $\hat{a}_i$ are scattered back from the preprocessing step. The preprocessing of modes allows a nonlocal measurement by combining the modes $\hat{b}_i$ with beam splitters and phase shifters. We denote the origin of the coordinate system on the detection plane as $\mathcal{O}$. All the components of the vectors are donated in the coordinate system $\mathcal{R}=(\mathcal{O},\hat{e}_x,\hat{e}_y,\hat{e}_z)$.

We introduced a shift in the denominator "$i\epsilon$" that is necessary for the integral to converge at $t=-\infty$.

B. State received by the antennas

The electromagnetic field is received by an interferometer that has an array of antennas, localized at positions $\mathbf{r}_i$ in a plane. The detection plane of antennas is parallel to the source plane and separated from it by a distance R (see Fig. 1). Each antenna is connected at its output to a waveguide that channels the received electromagnetic field radiation towards the measurement instruments. Receiver "i" consists of antenna "i" combined with its output waveguide. Its output, possibly after filtering, is assumed to be single mode with discrete annihilation operator $\hat{b}_i$. We call the modes received by the antennas "spatial field modes" since each mode $\hat{b}_i$ is specific to a location on the detection plane. Single modes with discrete annihilation operator $\hat{a}_i$ are reflected from the preprocessing stage. On the antenna side, we represent incoming plane waves in the interferometer by $\hat{a}(\mathbf{k},\sigma)$ and scattered outgoing plane waves by $\hat{b}(\mathbf{k},\sigma)$ (see Fig. 1). One can use the scattering matrix formalism to find the relation between incoming and outgoing modes.

Furthermore, the modes $\hat{b}_i$ are separated by distances substantially larger than the central wavelength λ. And the collection area of each antenna A_D is assumed to be $A_D\sim\lambda^2$, where λ is central wavelength. These constraints make the modes for different receivers orthogonal and simplifies the form of the scattering matrix. A scattering matrix connects incoming and outgoing modes, and one can write it as [62,63]

$$\mathcal{S}=\begin{bmatrix}\mathcal{S}^{(\text{scat})} & \mathcal{S}^{(\text{trans})}\\ \mathcal{S}^{(\text{rec})} & \mathcal{S}^{(\text{refl})}\end{bmatrix}. \tag{11}$$

This matrix acts on the vector $[\{\hat{a}(\mathbf{k},\sigma)\}_{\{\mathbf{k},\sigma\}},\{\hat{a}_i\}_{\{i\}}]^T$, where $\{a(\mathbf{k},\sigma)\}_{\{\mathbf{k},\sigma\}}$ is the vector of continuous plane-wave operators with continuous $\mathbf{k}$ and two polarizations. $\{\hat{a}_i\}_{\{i\}}$ is the vector of modes with $i\in\{1,\dots,n\}$ for an n-mode interferometer. The first block, $\mathcal{S}^{(\text{scat})}$, describes the scattering of incoming plane waves to outgoing plane waves from the interferometer. A receiver can receive or transmit the signal. The off-diagonal block $\mathcal{S}^{(\text{rec})}$ describes the coupling of the incoming plane waves $\hat{a}(\mathbf{k},\sigma)$ into the receiver modes $\hat{b}_i$, and $\mathcal{S}^{(\text{trans})}$ describes scattering of reflected receiver modes $\hat{a}_i$ into outgoing plane waves $\hat{b}(\mathbf{k},\sigma)$. The matrix $\mathcal{S}^{(\text{refl})}$ represents the scattering (reflection) between the receivers, and will be neglected, $\mathcal{S}^{(\text{refl})}\sim 0$. One can also verify that if the receivers have only incoming and outgoing modes, the receiving and transmitting pattern of the receivers will be the same $\mathcal{S}^{(\text{trans})}(\mathbf{k},\sigma;j)=\mathcal{S}^{(\text{rec})}(j;\mathbf{k},\sigma)$ and we can denote them as simply $\mathcal{S}_j(\mathbf{k},\sigma)$. Formally, the input-output relations read as

$$\hat{b}(\mathbf{k},\sigma)=\sum_{\sigma'}\int d^3\mathbf{k}'\mathcal{S}^{(\text{scat})}(\mathbf{k},\mathbf{k}',\sigma,\sigma')\hat{a}(\mathbf{k}',\sigma')+\sum_j\mathcal{S}_j(\mathbf{k},\sigma)\hat{a}_j \tag{12}$$

and

$$\hat{b}_i=\sum_{\sigma}\int d^3\mathbf{k}\,\mathcal{S}_i(\mathbf{k},\sigma)\hat{a}(\mathbf{k},\sigma). \tag{13}$$

For a lossless system we assume that $S^\dagger S=I$. Then we write $\mathcal{S}^{(\text{scat})}(\mathbf{k},\mathbf{k}',\sigma,\sigma')=(\mathcal{S}^{(\text{scat})})^T(\mathbf{k}',\mathbf{k},\sigma',\sigma)$. The field operators $\hat{a}(\mathbf{k},\sigma)$ from the state that we have for Eq. (7) can be replaced by the following relation for n different receiver modes:

$$\hat{a}(\mathbf{k},\sigma)=\sum_j^n\mathcal{S}_j^*(\mathbf{k},\sigma)\hat{b}_j+\sum_{\sigma'}\int d^3\mathbf{k}'\mathcal{S}^{*(\text{scat})}(\mathbf{k}',\sigma',\mathbf{k},\sigma)\hat{b}(\mathbf{k}',\sigma'). \tag{14}$$

The interferometer does not have any access to modes $\hat{b}(\mathbf{k},\sigma)$. Assuming that all antennas are identical in terms of their receiver pattern, except for their position $\mathbf{r}_i$ on the detection plane, each scattering function may be written as [62,63]

$$\mathcal{S}_i(\mathbf{k},\sigma)=e^{i(\mathbf{k}\cdot\mathbf{r}_i-\omega t_i)}\mathcal{S}(\mathbf{k},\sigma), \tag{15}$$

where t_i is the time at which we consider the state of the ith antenna. Since we are only interested in spatial modes, we assume that relative time differences between any pair of antennas is zero. Then we write $t_i\equiv\bar{t}$, with $\bar{t}$ the time when the signal from $(\mathbf{r},t)$ arrives at central antenna. And $\mathcal{S}(\mathbf{k},\sigma)$ is the function describes scattering to the central receiver. According to (14), t is the last time the current densities to be sensed imprint their information the coherent state labels $\alpha(\boldsymbol{k},\sigma)$. Further, the commutation relation of different receiver modes can be written as

$$[\hat{b}_i, \hat{b}_j^\dagger] = \sum_\sigma \int d^3\mathbf{k}\, \mathcal{S}_i(\mathbf{k}, \sigma)\mathcal{S}_j^*(\mathbf{k}, \sigma) \approx \delta_{ij}, \tag{16}$$

where we have used the canonic commutation relation of $\hat{a}(\mathbf{k}, \sigma)$ and we assumed that $|\mathcal{S}(\mathbf{k}, \sigma)|$ varies slowly compared to the oscillations of the exponential factor $\exp[i\mathbf{k} \cdot (\mathbf{r}_i - \mathbf{r}_j)]$ for $i \neq j$. Since $\hat{b}_i$ commutes with $\hat{b}(\mathbf{k}, \sigma)$, using Eq. (14) we can write the coherent state in Eq. (7) as

$$|\psi(t)\rangle = D(\{\beta_i\})D[\{\beta(\mathbf{k}, \sigma)\}]|\{0\}\rangle, \tag{17}$$

where $D[\{\beta(\mathbf{k}, \sigma)\}]$ can be defined similarly to Eq. (5) and $\beta(\mathbf{k}, \sigma)$ is the eigenvalue of the scattered plane-wave modes with annihilation operator $\hat{b}(\mathbf{k}, \sigma)$. Since the interferometer does not have any access to these modes, we can safely trace them out. The displacement operator for the spatial modes of the interferometer can be written in the form

$$D(\{\beta_i\}) = \bigotimes_i^n \exp[\beta_i \hat{b}_i^\dagger - \beta_i^* \hat{b}_i]. \tag{18}$$

Then we have a coherent state for spatial modes of the interferometer,

$$\rho' = |\{\beta_i\}\rangle\, \langle\{\beta_i\}|\,, \tag{19}$$

where

$$\beta_i = \sum_\sigma \int d^3k\, \mathcal{S}_i(\mathbf{k}, \sigma)\alpha(\mathbf{k}, \sigma). \tag{20}$$

$\mathcal{S}_i(\mathbf{k}, \sigma)$ depends on the type of receivers. Let us assume that each receiver is characterized by a filter function $w(\omega)$ with central frequency ω_0 and bandwidth $B \ll \omega_0$:

$$w(\omega) = \begin{cases} 1 & \text{for } \omega_0 - B/2 \leqslant \omega \leqslant \omega_0 + B/2, \\ 0 & \text{elsewhere.} \end{cases} \tag{21}$$

For simplicity we assume $\mathcal{S}(\mathbf{k}, \sigma) \propto \sqrt{\omega} w(\omega)\boldsymbol{\varepsilon}(\mathbf{k}, \sigma) \cdot \hat{u}$, and normalized according to Eq. (16) as

$$\mathcal{S}(\mathbf{k}, \sigma) = \left(\frac{3c^3\omega}{8\pi\omega_0^3 B}\right)^{1/2} w(\omega)\boldsymbol{\varepsilon}(\mathbf{k}, \sigma) \cdot \hat{u}, \tag{22}$$

where $\omega = c|\mathbf{k}|$ and $\hat{u}$ is the unit polarization direction of the corresponding receiver mode. Since we are using a filter function and $\mathcal{S}(\mathbf{k}, \sigma)$ is normalized, choosing $\sqrt{\omega}$ or with a different power will not change the result in Eq. (28). Yet, in Eq. (25) we have the term $\sim\omega\tilde{\mathbf{j}}_t(\mathbf{r}, \omega)$ by this choice and it is consistent with the van Cittert–Zernike theorem given in Ref. [42]. Then we have

$$\begin{aligned} \beta_i =& -\left(\frac{3c^3}{2^8\hbar\varepsilon_0\pi^5\omega_0^3 B}\right)^{1/2} \int d^3r \int_{-\infty}^{\infty} d\tilde{\omega} \\ &\times \sum_\sigma \int d^3k\, w(\omega)\tilde{\mathbf{j}}(\mathbf{r}, \tilde{\omega}) \cdot \boldsymbol{\varepsilon}(\mathbf{k}, \sigma)\boldsymbol{\varepsilon}(\mathbf{k}, \sigma) \cdot \hat{u} \\ &\times \frac{e^{i(\tilde{\omega}t + \omega t - \omega\bar{t})}e^{-i\mathbf{k}\cdot(\mathbf{r}-\mathbf{r}_i)}}{i\epsilon - c|\mathbf{k}| - \tilde{\omega}}. \end{aligned} \tag{23}$$

To take the integral over d^3k we align the k_z axis with the vector $(\mathbf{r} - \mathbf{r}_i)$. In spherical coordinates in k space we have $d^3k = \omega^2/c^3 d\omega\, d\Omega$, where $\omega = |\mathbf{k}|c$ and $\mathbf{k} = (\omega/c)\hat{\mathbf{n}}(\Omega)$ with $\hat{\mathbf{n}}(\Omega) = (\sin\theta\cos\phi, \sin\theta\sin\phi, \cos\theta)$. The frequencies will be filtered out by the filter function $w(\omega)$ and later only the integral over the surface from a distance R will be considered in the far-field regime $(R\omega_0/c \gg 1)$. Then in this step, we can drop the terms of order $1/f^2$ and $1/f^3$ with $f \equiv \omega|\mathbf{r} - \mathbf{r}_i|/c$. Taking the integral over Ω, summing over two polarizations, considering that our problem is limited to far field we have

$$\begin{aligned} \beta_i =& i\left(\frac{3c\mu_0}{64\hbar\pi^3\omega_0^3 B}\right)^{1/2} \int d^3r \int_{-\infty}^{\infty} d\tilde{\omega} \int_0^{\infty} d\omega\, w(\omega)\omega \\ &\times \tilde{\mathbf{j}}_t(\mathbf{r}, \tilde{\omega}) \cdot \hat{u} \frac{e^{i\omega|\mathbf{r}-\mathbf{r}_i|/c} - e^{-i\omega|\mathbf{r}-\mathbf{r}_i|/c}}{|\mathbf{r} - \mathbf{r}_i|} \frac{e^{i(\tilde{\omega}t + \omega t - \omega\bar{t})}}{i\epsilon - \omega - \tilde{\omega}}, \end{aligned} \tag{24}$$

where $\tilde{\mathbf{j}}_t(\mathbf{r}, \tilde{\omega})$ is the locally transverse component of the current density defined as $\tilde{\mathbf{j}}_t = \tilde{\mathbf{j}} - (\tilde{\mathbf{j}} \cdot \hat{e}_\mathbf{r})\hat{e}_\mathbf{r}$ with unit vector $\hat{e}_\mathbf{r} = (\mathbf{r} - \mathbf{r}_i)/|\mathbf{r} - \mathbf{r}_i|$. For $R \gg |\mathbf{r}_i|$, we have $\hat{e}_\mathbf{r} \approx \mathbf{r}/|\mathbf{r}|$, with corrections modifying only slightly the prefactors, not the phases. One can extend the lower bound of the integration range of the ω integral to $-\infty$ using the definition of $w(\omega)$, and evaluate the ω integral with the help of the law of residues. Since $\bar{t} > t - |\mathbf{r} - \mathbf{r}_i|/c$, the pole at $\omega = -\tilde{\omega} + i\epsilon$ contributes to the term $\exp(i\omega|\mathbf{r} - \mathbf{r}_i|/c)$. For $\exp(-i\omega|\mathbf{r} - \mathbf{r}_i|/c)$ the contour must be closed in the lower half-plane and there is no pole to contribute. In the end one should send $\epsilon \to 0$. Then β_i simplifies to

$$\begin{aligned} \beta_i = & -\left(\frac{3c\mu_0}{16\pi\hbar\omega_0^3 B}\right)^{1/2} \int_{-\infty}^{\infty} d\omega\, w(-\omega)\omega \int d^3r \\ &\times \tilde{\mathbf{j}}_t(\mathbf{r}, \omega) \cdot \hat{u} \frac{e^{-i\omega(\bar{t} - |\mathbf{r}-\mathbf{r}_i|/c)}}{|\mathbf{r} - \mathbf{r}_i|}, \end{aligned} \tag{25}$$

where we drop the "$\sim$" from $\tilde{\omega}$. The state in Eq. (7) is written for a deterministic current density distribution. In reality, these current densities fluctuate. Before we move forward, we describe the properties of this current density distribution. We assume that it is a complex symmetric Gaussian process with current densities uncorrelated in positions, directions, and frequencies [43,64,65],

$$\begin{aligned} &\langle\tilde{j}_l(\mathbf{r}, \omega)\tilde{j}_m^*(\mathbf{r}', \omega')\rangle = \frac{l_c^3}{\tau_c}\delta_{lm}\delta(\omega - \omega')\delta(\mathbf{r} - \mathbf{r}')\,\langle|\tilde{j}_l(\mathbf{r}, \omega)|^2\rangle\,, \\ &\langle\tilde{j}_l(\mathbf{r}, \omega)\tilde{j}_m(\mathbf{r}', \omega')\rangle = 0, \quad \langle\tilde{j}_l^*(\mathbf{r}, \omega)\tilde{j}_m^*(\mathbf{r}', \omega')\rangle = 0. \end{aligned} \tag{26}$$

The length scale l_c and timescale τ_c are introduced for dimensional grounds and the polarizations are indexed by l, m taking values x, y, z. For the classical white-noise currents Eq. (26) is a standard model, and appears in many places in the literature [66–68]. One can also derive Planck's law for the energy density of an electromagnetic field in thermal equilibrium from it (see Appendix of Ref. [43]). We choose the unit polarization vector of the receiver $\hat{u}$ as one of the basis vectors of the coordinate system $\mathcal{R}$ parallel to the detection plane, in either x or y direction. Then, we write $\langle\tilde{\mathbf{j}}_t(\mathbf{r}, \omega) \cdot \hat{u}\tilde{\mathbf{j}}_t^*(\mathbf{r}, \omega) \cdot \hat{u}\rangle = \langle|\tilde{j}_{t,l}(\mathbf{r}, \omega)|^2\rangle$. Using Eq. (19) and introducing the distribution of the current density $P(\tilde{j}(r, \omega))$, the state for the interferometer ρ_{int} with n receivers can be written as

$$\rho_{\text{int}} = \int d^2\tilde{j}\, P(\tilde{j}(\mathbf{r},\omega))|\{\beta_i\}\rangle\langle\{\beta_i\}|. \tag{27}$$

The integral is over the complex $\tilde{j}$ plane. Since it is a circularly symmetric Gaussian process, $P(\tilde{j}(\mathbf{r},\omega))$ is assumed through its moments given in Eq. (26). Gaussian states are completely characterized by their mean displacement $\Gamma_i = \text{Tr}[\rho\mathbf{b}_i]$ and covariance matrix with elements $\Sigma_{ij} = \frac{1}{2}\text{Tr}[\rho(\tilde{\mathbf{b}}_i\tilde{\mathbf{b}}_j + \tilde{\mathbf{b}}_j\tilde{\mathbf{b}}_i)]$, where $\mathbf{b} = [b_1, b_1^\dagger, b_2, b_2^\dagger, \dots, b_n, b_n^\dagger]$ and $\tilde{\mathbf{b}}_i = \mathbf{b}_i - \Gamma_i$ [26,69–73]. The mean displacement for our state is zero $\Gamma_i = 0$ considering Eq. (26). To find the elements of the covariance matrix, we need to calculate $\langle b_i^\dagger b_j\rangle$. The integral over ω can be taken using the filter function of bandwidth B. With this we find

$$\langle b_i^\dagger b_j\rangle = K\int d^3r\, \frac{\langle|\tilde{j}_{t,l}(\mathbf{r},\omega)|^2\rangle\, e^{i\omega_0(|\mathbf{r}-\mathbf{r}_j|-|\mathbf{r}-\mathbf{r}_i|)/c}}{|\mathbf{r}-\mathbf{r}_i||\mathbf{r}-\mathbf{r}_j|} \times \text{sinc}\left[\frac{B}{2c}(|\mathbf{r}-\mathbf{r}_j| - |\mathbf{r}-\mathbf{r}_i|)\right], \tag{28}$$

where $K = 3c\mu_0 l_c^3/(16\pi\hbar\omega_0\tau_c)$ and $\text{sinc}[x] \equiv \sin x/x$. For a very narrow bandwidth $\text{sinc}[\dots] \approx 1$. Then, Eq. (28) for $i = j$ becomes

$$\bar{n} = K\int d^3r\, \frac{\langle|\tilde{j}_{t,l}(\mathbf{r},\omega)|^2\rangle}{|\mathbf{r}-\mathbf{r}_i|^2}, \tag{29}$$

where we defined $\bar{n} \equiv \langle b_i^\dagger b_i\rangle$ without any index since the mean photon number is the same for all interferometer modes in the far-field approximation, and for $i \neq j$ it becomes

$$\xi_{ij} = K\int d^3r\, \frac{\langle|\tilde{j}_{t,l}(\mathbf{r},\omega)|^2\rangle\, e^{i\omega_0(|\mathbf{r}-\mathbf{r}_j|-|\mathbf{r}-\mathbf{r}_i|)/c}}{|\mathbf{r}-\mathbf{r}_i||\mathbf{r}-\mathbf{r}_j|} \tag{30}$$

with $\xi_{ij} \equiv \langle b_i^\dagger b_j\rangle$. The integral over Earth's surface is parametrized by $\mathbf{r} = (x, y, R)$ with respect to the coordinate system of the detection plane. Further, we write $|\mathbf{r}-\mathbf{r}_j| - |\mathbf{r}-\mathbf{r}_i| \approx \Delta\mathbf{r}_{ij}\cdot\mathbf{r}/|\mathbf{r}|$ for $|\Delta\mathbf{r}_{ij}| \ll R$, where $\Delta\mathbf{r}_{ij} = \mathbf{r}_j - \mathbf{r}_i$ connects two different receiver modes. In the denominator, we approximate $|\mathbf{r}-\mathbf{r}_i| \approx R/\cos\tilde{\theta}(x,y)$ with $\tilde{\theta}(x,y)$ the polar angle the angle between the z axis and the vector (x, y, R). One can relate the average amplitude of current density to brightness temperature $T_{\text{B}}(x,y)$ by $\langle|\tilde{j}_{t,l}(\mathbf{r},\omega)|^2\rangle = K_1 T_{\text{B}}(x,y)\cos\tilde{\theta}(x,y)\delta(z-R)$ with a constant defined as $K_1 = 32\tau_c k_B/(3l_c^3\mu_0 c)$ (see Appendix A). We define the effective temperature as $T_{\text{eff}}(x,y) \equiv T_{\text{B}}(x,y)\cos^3\tilde{\theta}(x,y)$ and a new constant $\kappa = K_1 K \equiv 2k_B/(\pi\hbar\omega_0)$ where κ has the dimension of inverse temperature with SI units "1/K." Then we can simplify Eq. (29) for $i = j$ as

$$\bar{n} = \frac{\kappa}{R^2}\int dx\,dy\,T_{\text{eff}}(x,y), \tag{31}$$

and for $i \neq j$ as

$$\xi_{ij} = \frac{\kappa}{R^2}\int dx\,dy\,T_{\text{eff}}(x,y)e^{2\pi i(v_x^{ij}x + v_y^{ij}y)}, \tag{32}$$

where

$$v_y^{ij} = \frac{\Delta x_{ij}}{\lambda R}, \qquad v_x^{ij} = \frac{\Delta y_{ij}}{\lambda R}. \tag{33}$$

We used $\omega_0/c = 2\pi/\lambda$. These two equations suffice to determine the covariance matrix elements of the Gaussian states for the general interferometer with an array of antennas. All spatial field modes received by the interferometer undergo a preprocessing before measurement. This processing can be understood as a linear combination of all spatial modes in such a way to achieve the optimal POVM for the best estimation of the parameter we are interested in (see Sec. II C). We use the values of the SMOS for the rest of the paper which leads to $\kappa \sim 9.4$ 1/K.

C. Quantum Cramér-Rao bound

A lower bound of an unbiased estimator of a deterministic parameter is given by the Cramér-Rao bound (CRB), which states that the variance of any such estimator is equal or greater than the inverse of the Fisher information. The quantum analog of the CRB is the quantum Cramér-Rao bound (QCRB), given by the inverse of the QFI. The significance of the QCRB lies in the fact that in the case of a single parameter to be estimated the bound can in principle be saturated in the limit of infinitely many measurements when choosing the optimal quantum measurement and maximum-likelihood estimation. Let us consider a quantum state $\rho_{\boldsymbol{\mu}}$ that depends on a vector of l parameters, $\boldsymbol{\mu} = (\mu_1, \mu_2, \dots, \mu_l)^T$. One can generalize the single-parameter QCRB [4,5] to the multiparameter QCRB [74] given for a single measurement by

$$\text{Cov}(\tilde{\boldsymbol{\mu}}) \geqslant \mathscr{F}(\boldsymbol{\mu})^{-1}, \quad \mathscr{F}_{ij}(\boldsymbol{\mu}) = \tfrac{1}{2}\,\text{tr}\,(\rho_{\boldsymbol{\mu}}\{\mathscr{L}_i, \mathscr{L}_j\}), \tag{34}$$

where $\text{Cov}(\tilde{\boldsymbol{\mu}})$ is a covariance matrix for the locally unbiased estimator $\tilde{\boldsymbol{\mu}}(x)$ [48,53], the $\{\cdot,\cdot\}$ means the anticommutator, and $\mathscr{L}_i$ is the symmetric logarithmic derivative (SLD) related to parameter i, which is defined similarly to the single-parameter case $\frac{1}{2}(\mathscr{L}_i\rho_{\boldsymbol{\mu}} + \rho_{\boldsymbol{\mu}}\mathscr{L}_i) = \partial_i\rho_{\boldsymbol{\mu}}$. For any given positive weight matrix $\boldsymbol{W}$, the estimation cost is bounded by $\text{Tr}[\boldsymbol{W}\,\text{Cov}(\tilde{\boldsymbol{\mu}})] \geqslant \text{Tr}[\boldsymbol{W}\mathscr{F}(\boldsymbol{\mu})^{-1}] \equiv C^S(\boldsymbol{\mu}, \boldsymbol{W})$. Contrary to the single-parameter case, the multiparameter QCRB can in general not be saturated. This problem was realized by Holevo [52]. He proposed a tighter and more fundamental bound $C^H(\boldsymbol{\mu}, \boldsymbol{W})$, which is upper bounded by $2C^S(\boldsymbol{\mu}, \boldsymbol{W})$ [75,76]. In case of the asymptotically classical models, where SLD operators for different parameters commute on average $\text{Tr}(\rho_{\boldsymbol{\mu}}[L_i, L_j]) = 0$, the Holevo CRB is equivalent to the QCRB and it can be saturated asymptotically with a collective measurement on an asymptotically large number of copies $\rho_{\boldsymbol{\mu}}^{\otimes\mathcal{N}}$ [53,76].

The SLD and the elements of QFI matrix are given in Ref. [71] for any Gaussian state. The SLD can be written as

$$\mathscr{L}_i = \tfrac{1}{2}\mathfrak{M}^{-1}_{\alpha\beta,\gamma\delta}(\partial_i\Sigma^{\gamma\delta})(\mathbf{b}_\alpha\mathbf{b}_\beta - \Sigma^{\alpha\beta}), \tag{35}$$

where the summation convention is used. In our case, the mean displacement of Gaussian state is zero. Thus, we can simplify further the elements of the QFI matrix in [71] to

$$\mathscr{F}_{ij} = \tfrac{1}{2}\mathfrak{M}^{-1}_{\alpha\beta,\gamma\delta}\partial_j\Sigma^{\alpha\beta}\partial_i\Sigma^{\gamma\delta}, \tag{36}$$

where

$$\mathfrak{M} \equiv \Sigma\otimes\Sigma + \tfrac{1}{4}\Omega\otimes\Omega, \tag{37}$$

and $\Omega = \bigoplus_{k=1}^{n} i\sigma_y$. Using the properties of the Gaussian state (circularly symmetric and with zero mean) we can write the SLD for n-mode interferometers as

$$\mathscr{L}_i = \sum_{j}^{n} g_i^j \hat{b}_j^\dagger \hat{b}_j + \sum_{j<k}^{n} \left(g_i^{jk} \hat{b}_j^\dagger \hat{b}_k + \left(g_i^{jk}\right)^* \hat{b}_k^\dagger \hat{b}_j \right) + \mathrm{C}, \tag{38}$$

where C is a constant term. In the single-parameter case, the optimal POVM is the set of projectors onto eigenstates of $\mathscr{L}_i$. It allows one to saturate the QCRB in the limit of infinitely many measurements and maximum-likelihood estimation [4,77,78]. For the diagonalization of the SLD, the constant C is not important and we can drop it from the beginning. We construct a Hermitian matrix $\mathbf{M}_i$

$$\mathbf{M}_i = \begin{bmatrix} g_i^1 & g_i^{12} & \dots & g_i^{1n} \\ (g_i^{12})^* & g_i^2 & \dots & g_i^{2n} \\ \dots & \dots & \dots & \dots \\ (g_i^{1n})^* & (g_i^{2n})^* & \dots & g_i^n \end{bmatrix}, \tag{39}$$

where the diagonal elements are real-valued functions which can be defined as $g_i^j = \mathfrak{M}^{-1}_{\alpha\beta,\gamma\delta}(\partial_i \Sigma^{\gamma\delta})$ with $\alpha = 2j$ and $\beta = 2j - 1$. The off-diagonal elements are complex-valued functions which are defined as $g_i^{jk} = \mathfrak{M}^{-1}_{\alpha\beta,\gamma\delta}(\partial_i \Sigma^{\gamma\delta})$ with $\alpha = 2j$ and $\beta = 2k - 1$ and $k > j$. Further, we can define a new set of operators $\bar{\mathbf{b}}^\dagger \equiv [\hat{b}_1^\dagger, \hat{b}_2^\dagger, \dots, \hat{b}_n^\dagger]$ and $\bar{\mathbf{b}} \equiv [\hat{b}_1, \hat{b}_2, \dots, \hat{b}_n]^T$. Then the SLD becomes

$$\mathscr{L}_i = \bar{\mathbf{b}}^\dagger \mathbf{M}_i \bar{\mathbf{b}}. \tag{40}$$

Since $\mathbf{M}_i$ is a Hermitian matrix, it can always be unitarily diagonalized by $\mathbf{M}_i = \mathbf{V}_i^\dagger \mathbf{D}_i \mathbf{V}_i$ with $\mathbf{V}_i^\dagger \mathbf{V}_i = I$. A new set of operators can be defined as $\bar{\mathbf{d}}_i^\dagger = \bar{\mathbf{b}}^\dagger \mathbf{V}_i^\dagger$ where $\bar{\mathbf{d}}_i^\dagger = [\hat{d}_{i1}^\dagger, \hat{d}_{i2}^\dagger, \dots, \hat{d}_{in}^\dagger]$. The optimal POVM for the single-parameter case ($i = 1$, which we drop in the following) can be found as a set of projectors in the Fock basis $\{|m_1, m_2, \dots, m_n\rangle \langle m_1, m_2, \dots, m_n|\}_{\{m_1, m_2 \dots m_n\}}$ of the $\hat{d}_l$ with $\hat{d}_l^\dagger \hat{d}_l \, |m_1, m_2, \dots, m_n\rangle = m_l \, |m_1, m_2, \dots, m_n\rangle$, where $l \in \{1, \dots, n\}$. The $\hat{d}_l$ will be called "detection modes." In the case of multiparameter estimation, one needs to check the compatibility conditions to saturate the SLD-CRB. Thus, we give the general commutation relation of SLD in Appendix B for an n-mode interferometer. We see that the SLDs for $n < 3$ commute on average, $\mathrm{Tr}\,[\rho_{\mathrm{int}}[\mathscr{L}_i, \mathscr{L}_j]] = 0$, for any parameter estimation.

III. RESULTS

A. Single receiver

In this section, we consider the case of the simplest estimation of the parameters of the sources with a single receiver with mode $\hat{b}$. Then the covariance matrix for the state can be written as

$$\Sigma = \begin{bmatrix} 0 & \chi \\ \chi & 0 \end{bmatrix}. \tag{41}$$

The QFI matrix elements for single mode can be found as

$$\mathscr{F}_{ij} = \frac{4\partial_i \chi \partial_j \chi}{4\chi^2 - 1}, \tag{42}$$

and, up to the irrelavant constant, the SLD becomes

$$\mathscr{L}_i = \frac{4\partial_i \chi}{4\chi^2 - 1} \hat{b}^\dagger b. \tag{43}$$

Since the SLD is already diagonal in the basis of $\hat{b}^\dagger \hat{b}$, the detection mode can be considered as $\hat{b}$. We write the POVM obtained from the SLD as a set of projectors in the Fock basis $\{|m\rangle \langle m|\}_{\{m\}}$ which is the eigenbasis of $\hat{b}^\dagger \hat{b}$, $\hat{b}^\dagger \hat{b} \, |m\rangle \langle m| = m \, |m\rangle \langle m|$. To compare, we consider the POVM from heterodyne detection. The heterodyne detection uses a classical local oscillator to make a measurement locally on the basis of coherent states. For a single mode, its POVM elements can be written as $E(\nu) = |\nu\rangle \langle \nu| / \pi$ where $|\nu\rangle$ is coherent state and $\int d^2\nu \, E(\nu) = \mathbb{1}$. The probability that $E(\nu)$ triggers reads as

$$P(\nu|\mu_i) = \frac{1}{\pi(1 + \bar{n})} \exp\left[-\frac{|\nu|^2}{(1 + \bar{n})} \right], \tag{44}$$

with $\bar{n}$ given by Eq. (31). The classical Fisher information (CFI) for parameter μ_i can be written as

$$F_i = \int d^2\nu \frac{1}{P(\nu|\mu_i)} \left(\frac{\partial P(\nu|\mu_i)}{\partial \mu_i} \right)^2. \tag{45}$$

Resolution of a uniform circular source. Consider a source defined as a circular disk with radius a and with uniform temperature T located under the interferometer at a distance R [$\mathbf{r} = (0, 0, R)$]. We are interested in estimating a or T. While estimating one of them, we will assume that the other parameter is known to sufficiently large precision. The temperature distribution on the source plane becomes

$$T_{\mathrm{eff}}(x, y) = T \;\mathrm{circ}(x, y), \tag{46}$$

where the symbol circ(·) stands for the circular function, defined as

$$\mathrm{circ}(x, y) \triangleq \begin{cases} 1, & \sqrt{x^2 + y^2} \leqslant a \\ 0, & \sqrt{x^2 + y^2} > a. \end{cases} \tag{47}$$

We assume $a \ll R$. Then only small angles are involved and one can set $\cos^3 \Theta(x, y) \approx 1$. This corresponds to one of the approximations characteristic of the far-field regime [79]. Using Eq. (31), we have $\bar{n} = \pi a^2 \kappa T / R^2$ and $\chi = 1/2 + \bar{n}$. The QFI for estimating a becomes

$$\mathscr{F}_a = \frac{4\pi T \kappa}{R^2 + a^2 \pi T \kappa}. \tag{48}$$

Then we can write the SLD for estimating the a ignoring the constant term as

$$\mathscr{L}_a = \frac{2R^2}{aR^2 + a^3 \pi T \kappa} \hat{b}^\dagger \hat{b}. \tag{49}$$

The CFI of the heterodyne detection becomes

$$F_a = \frac{4a^2 \pi^2 T^2 \kappa^2}{(R^2 + a^2 \pi T \kappa)^2}. \tag{50}$$

In Fig. 2, we compare the QFI with the CFI of heterodyne detection. As one can see, for small source sizes, the Fisher information from heterodyne measurement vanishes. However, the QFI tends to a constant. For instance, in the limit $a \to 0$, for $T = 300$ K we have QFI for estimating a as $\mathscr{F}_a \sim 6.16 \times 10^{-2}$ 1/km^2, which gives a smallest standard

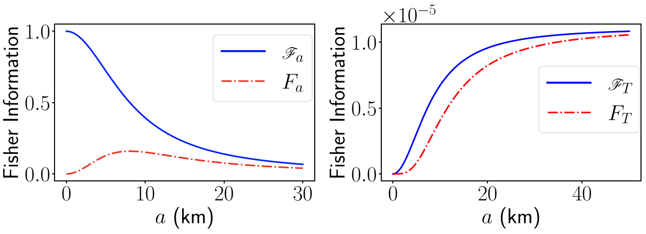

(a) (b)

FIG. 2. (a) The QFI (solid blue line) and the CFI (dotted-dashed red line) from the heterodyne measurement to estimate the source size as a function of a. Both results are dimensionless and scaled with the $4\pi T\kappa/R^2$, considering $T = 300$ K. (b) The QFI (solid blue line) and the CFI (dotted-dashed red line) from the heterodyne measurement to estimate the temperature as a function of a. Both results are in units of $1/\mathrm{K}^2$, and we consider $T = 300$ K.

deviation of about 4 km. Thus, we can conclude that the photon-number measurement on the complete basis of Fock states in the detection mode $\hat{b}$ helps us to get better resolution than heterodyne measurement. If a becomes larger, we can see that the QFI and CFI get close to each other at some point. To estimate a, we assumed that we know exactly the temperature of the source. Further, we find the QFI for estimating the temperature as

$$\mathscr{F}_T = \frac{\pi a^2 \kappa}{R^2 T + a^2 \pi T^2 \kappa}, \tag{51}$$

with a SLD given by

$$\mathscr{L}_T = \frac{R^2}{T R^2 + a^2 \pi T^2 \kappa} \hat{b}^\dagger \hat{b}. \tag{52}$$

The optimal POVM is a set of projectors in the Fock basis $\{|m\rangle\langle m|\}_{\{m\}}$ for both estimating a and T. The CFI from heterodyne detection to estimate temperature becomes

$$F_T = \frac{\pi^2 a^4 \kappa^2}{(R^2 + a^2 \pi T\kappa)^2}. \tag{53}$$

In Fig. 2(b), we plot both QFI and CFI for heterodyne detection for temperature estimation. Both have very close functional behavior. They vanish for $a \to 0$ and they approach each other when we have a large source size.

The off-diagonal matrix element of the QFI matrix for multiparameter estimation reads as

$$\mathscr{F}_{aT} = \frac{2a\pi\kappa}{R^2 + a^2 \pi T\kappa}. \tag{54}$$

By sampling the same state $\mathcal{N}$ times, the standard deviation of the estimator decreases proportional to $1/\sqrt{\mathcal{N}}$. The SMOS satellite moves at a constant speed $v \simeq 7$ km/s and takes the time $\tau = L/v$ to fly over a distance L. For each sample there is a lower bound for the detection time given by $t_D \sim 1/B$ (see Appendix A). In practice, the effective detection time might be much larger, due to, e.g. dead times of the detectors, slow electronics, etc. In addition, zero temperature of the detector and modes b_i is implicitly assumed in our calculations, but would require cooling down to temperatures much smaller than $\hbar\omega_0$. If the actual detection time is t_D^{eff}, the sample size becomes $\mathcal{N} = \tau/t_D^{\mathrm{eff}}$. In this paper we intend to establish the ultimate theoretical bounds and hence assume that the minimal detection time $t_D = 1/B$ can be achieved, in which case the sample size becomes $\mathcal{N} \sim LB/v$. To estimate the source size one can assume that $L \sim a$, and the QCRB for estimating a becomes $\delta a \geqslant 1/\sqrt{\mathcal{N}\mathcal{F}_a}$. Since $\mathcal{N}$ depends also on a one can find the optimum bound in the sense of a minimal δa at $a = R/\sqrt{\pi\kappa T}$. For $T = 300$ K, we find $a \sim 7.9$ km and $\delta a \gtrsim 1.0$ m. The bound for estimating T, assuming all other parameters known, can be written as $\delta T \geqslant 1/\sqrt{\mathcal{N}\mathcal{F}_T}$. Using the same parameters as before and the same sample size, we have $\delta T \gtrsim 0.08$ K. Thus, increasing the sample size to the theoretically maximally possible value, the spatial resolution improves by a factor of order 35 000 compared to the resolution of SMOS, and the radiometric resolution by factor of order 500. One can also increase the resolution by increasing the number of antennas, which we present in the following sections.

B. Two-mode interferometer

The optimum measurement with a two-mode interferometer for temperature estimation of a black body was considered in Ref. [80] and experimentally demonstrated in Ref. [81]. Further, the spatial resolution of two equally bright point sources with a similar setup was recently studied in Ref. [35]. In the previous section, we only considered a single receiver with mode $\hat{b}$. It is obvious that we may get additional information from the cross correlations of an n-mode interferometer. An analytical calculation of the QFI matrix for n-mode interferometer generally becomes untractable for $n > 2$ and one has to rely on numerical calculation (see Sec. III C). In this section, we consider two receivers with modes $\hat{b}_1$ and $\hat{b}_2$ to analyze the estimation of a single uniform circular disk for its size a and temperature T and two uniform circular disks with different temperatures for their the spatial resolution (source separation s_i and centroid t_i with $i \in \{x, y\}$). We write $\mathbf{b}$ as $\mathbf{b}^\top = (\hat{b}_1, \hat{b}_1^\dagger, \hat{b}_2, \hat{b}_2^\dagger)$. Since, the mean displacement is $\Gamma_i = 0$, the covariance matrix Σ of the state ρ_{int} becomes

$$\Sigma = \begin{bmatrix} 0 & \chi & 0 & \xi \\ \chi & 0 & \xi^* & 0 \\ 0 & \xi^* & 0 & \chi \\ \xi & 0 & \chi & 0 \end{bmatrix}, \tag{55}$$

where $\chi = 1/2 + \bar{n}$ and $\xi = \langle b_2^\dagger b_1 \rangle$. We give the general result for the QFI elements in Appendix C. Further, one can write the matrix $\mathbf{M}_i$ as

$$\mathbf{M}_i = \begin{bmatrix} g_i^1 & |g_i^2| e^{i\delta_i} \\ |g_i^2| e^{-i\delta_i} & g_i^1 \end{bmatrix}, \tag{56}$$

where g_i^1, g_i^2 are given in Appendix C in terms of χ and ξ, and δ_i is the phase difference between two modes in the SLD. Using the eigenvectors of $\mathbf{M}_i$, we can write the unitary $\mathbf{V}_i$ as

$$\mathbf{V}_i = \frac{1}{\sqrt{2}} \begin{bmatrix} 1 & e^{i\delta_i} \\ 1 & -e^{i\delta_i} \end{bmatrix}. \tag{57}$$

We see that $\mathbf{V}_i$ does not depend on the magnitude of the elements of the matrix $\mathbf{M}_i$ for a two-mode interferometer. The detection modes can be found as $\hat{d}_1 = (\hat{b}_1 + \hat{b}_2 e^{i\delta_i})/\sqrt{2}$ and $\hat{d}_2 = (\hat{b}_1 - \hat{b}_2 e^{i\delta_i})/\sqrt{2}$. The preprocessing to combine these two modes can be done by a phase delay on one of the modes

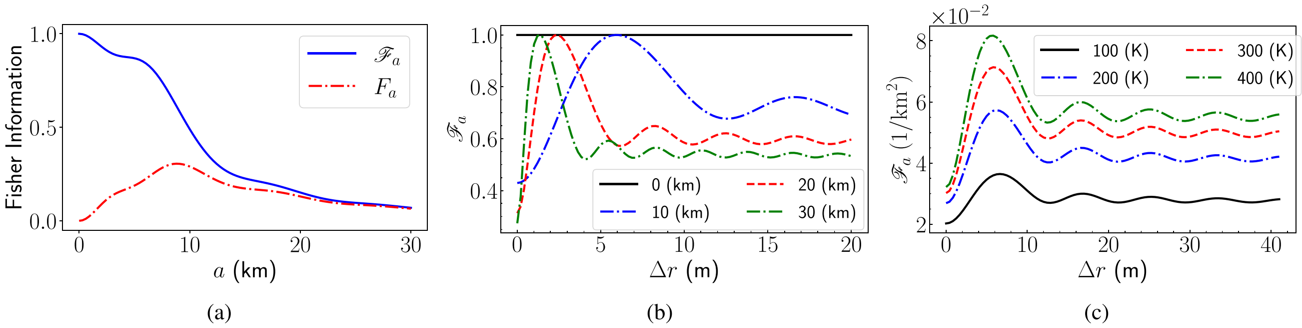

FIG. 3. (a) The QFI (solid blue) and the CFI (dotted-dashed red) from the heterodyne measurement to estimate the source size as a function of a. Both of the results are scaled with Eq. (59). In the limit $a \to 0$, for $T = 300$ K we have $\mathscr{F}_a \sim 0.117$ 1/km^2, which gives us a standard deviation around 2.92 km. (b) The QFI $\mathscr{F}_a$ for estimating the size of the circular disk as a function of Δr (spatial separation of two receivers) for different source sizes $a = (0, 10, 20, 30)$ km with $T = 300$ K. Data are scaled by the maximum values of the QFI, which are $\sim$0.117, $\sim$ 0.070, $\sim$ 0.030, $\sim$ 0.015 1/km^2, respectively. (c) The QFI $\mathscr{F}_a$ for estimating the size of the circular disk as a function of separation of two antennas Δr, for different temperatures T.

and then combining these modes by a beam splitter before any measurement. Then the POVM for the optimum measurement can be written as a set of projectors again in Fock basis as $\{|m_1, m_2\rangle \langle m_1, m_2|\}_{\{m_1,m_2\}}$ which is the eigenbasis of $\hat{d}_l^\dagger \hat{d}_l$, $\hat{d}_l^\dagger \hat{d}_l\, |m_1, m_2\rangle = m_l\, |m_1, m_2\rangle$. We check the weak compatibility condition for the SLD operators for general ith and jth parameters of two-mode interferometer in Appendix B. We find that the SLD operators commute on average on ρ_{int}, $\text{Tr}[\rho_{\text{int}}[\mathscr{L}_i, \mathscr{L}_j]] = 0$ for the two-mode interferometer. In this case, $C^H(\boldsymbol{\mu}, \boldsymbol{W}) = C^S(\boldsymbol{\mu}, \boldsymbol{W})\ \forall\ \boldsymbol{W}$ and the SLD-CRB can be saturated asymptotically by a collective measurement on an asymptotically large set of copies $\rho_{\text{int}}^{\otimes\mathcal{N}}$ of ρ_{int}. To compare this POVM with the classical approach, we consider heterodyne detection (see Appendix D).

Resolution of uniform circular source. Let us assume that on the source plane, we have a circular disk of radius a with uniform temperature T located at $\mathbf{r} = (x_0, y_0, R)$. Then the temperature distribution over the surface on the source plane can be written as $T_{\text{eff}}(x, y) = T\ \text{circ}(x - x_0, y - y_0)$. We want to estimate again a and T. The QFI for estimating the source size is given by Eq. (E4) for a two-mode interferometer. The expression is quite complicated. However, we can analyze it numerically, or we can look at certain limits. Estimating the size of the circle $\mathscr{F}_a$ depends on Δr (the separation of the two antennas). Physically we assumed this separation to be greater than the central wavelength $\Delta r > \lambda$. Mathematically, one can take the limit $\Delta r \to 0$, in which case the additional information from the phase difference between two antennas vanishes. In this limit, the QFI for estimating the source size becomes

$$\mathscr{F}_a \xrightarrow{\Delta r \to 0} \frac{8\pi\kappa T}{R^2 + 2\pi a^2 \kappa T}. \tag{58}$$

If we have $2\pi a^2 \kappa T \gg R^2$, the QFI for estimating a is $\mathscr{F}_a \sim 4/a^2$; for high temperatures or large a, the error of estimating the size of the source linearly increases with its size. Figure 3(b) shows how the QFI changes when we decrease the source size. In the limit of $a \to 0$, the QFI for estimating the source size becomes

$$\mathscr{F}_a \xrightarrow{a \to 0} \frac{8\pi\kappa T}{R^2}. \tag{59}$$

Comparing with the single receiver the QFI is doubled for two-mode interferometers in the limit $a \to 0$. We can still have nonvanishing QFI for $a \to 0$, as we can see from the black line in Fig. 3(b), which is the limit as in Eq. (59). The black line ($\sim$0 km source size) is scaled with $\sim$0.117 1/km^2, which corresponds to a standard deviation of $\sim$2.92 km for the interferometer with two modes. We give the CFI for heterodyne detection in Eq. (E14). For small source size, we can ignore the higher-order terms in a, and we can simplify it as

$$F_a \approx \frac{16\pi^2\kappa^2 T^2 a^2}{R^4}. \tag{60}$$

As we can see, for $a \to 0$, the CFI for heterodyne detection tends to zero. Thus, the resolution of the source size with heterodyne detection becomes arbitrarily bad in that limit [see Fig. 3(a)]. However, for large source sizes, we can see from Fig. 3(a) that CFI and QFI become equivalent. Therefore, constructing a POVM from the SLD can beat Rayleigh's resolution curse, even for estimating the source size. To construct the POVM for estimating the source size we give the elements of matrix $\mathbf{M}$ in Eqs. (E9) and (E10). The phase delay is found as $\delta_a = x_0 v_x + y_0 v_y$, with v_i defined as $v_x = \Delta r \cos\varphi/(\lambda R)$, $v_y = \Delta r \sin\varphi/(\lambda R)$. Thus, once we have the information of the location of the source centroid, we can combine these two interferometer modes by using a phase delay to get the POVM that saturates the QCRB. We plot the QFI as a function of Δr in Fig. 3(c) for different temperatures. We can see that when the effective temperature of the circular source increases, the QFI also increases. Moreover, when we increase Δr, the QFI for estimating a increases up to a maximum around $\Delta r \sim 6$ m. The reason for this is additional information coming from the phase differences in the two antennas. The QFI in Eq. (59) is doubled compared to QFI for single receiver in Eq. (48) in the limit $a \to 0$.

In the limit $\Delta r \to 0$, the QFI for estimating T becomes

$$\mathscr{F}_T \to \frac{2\pi a^2 \kappa}{T(2\pi a^2 \kappa T + R^2)}. \tag{61}$$

Since we assume we are in a microwave regime $k_B T \gg \hbar\omega_0$, we can not take the limit $T \to 0$. Instead, we can verify that the QFI for estimating the temperature depends on the source size for a finite temperature. Now, for $T = 300$ K and 30 km source size we have the QFI around 2×10^{-5} $1/\mathrm{K}^2$ which gives a very high standard deviation around 221 K. We show in the next section that the QFI also increases if we increase the number of spatial modes. For instance, for 20 antennas, we have QFI around 1.5×10^{-4} $1/\mathrm{K}^2$, and the standard deviation is 79 K for a single measurement.

In the limit $\Delta r \to 0$, the CFI from heterodyne detection becomes

$$F_T \to \frac{4\pi^2 a^4 \kappa^2 (\pi a^2 \kappa T + R^2)(3\pi a^2 \kappa T + R^2)}{(2\pi a^2 \kappa T + R^2)^4}. \tag{62}$$

To compare with the QFI we assume the brightness temperature $T = 300$ K and source size $a = 30$ km. This gives a CFI around 8×10^{-6} $1/\mathrm{K}^2$ which give us a standard deviation around 350 K. Compared to the QFI information, the CFI is around 2.5 times smaller. Therefore, combining the spatial modes (receivers) and measuring photon number in the Fock basis of $\hat{d}_1, \hat{d}_2$, as expected, is more advantageous even for estimating the temperature.

So far, we only gave the diagonal elements of the QFI matrix, relevant for estimating each parameter individually, assuming all other parameters are known. The single independent off-diagonal element of the QFI matrix regarding a and T is given in Eq. (E7). In the limit $\Delta r \to 0$ it simplifies to

$$\mathscr{F}_{aT} = \frac{4\pi a \kappa}{2\pi a^2 \kappa T + R^2}. \tag{63}$$

Then one can construct the QFI matrix to find the QCRB for multiparameter estimation. Further, we can estimate the source location considering the two parameters x_0, y_0. The QFI matrix elements for estimating the source locations can be written as

$$\mathscr{F}_{i_0 j_0} = \frac{8\pi^2 \Delta r^2 \kappa T J_1^2 v_i v_j}{\pi \Delta r^2 (\pi a^2 \kappa T + R^2) - \kappa \lambda^2 R^2 T J_1^2}, \tag{64}$$

where $i, j \in \{x, y\}$. The QFI for estimating the source location depends on source size and source temperature. Since the elements $\mathscr{F}_{i_0 a}$ and $\mathscr{F}_{i_0 T}$ of the QFI matrix are zero, source size and location can be estimated simultaneously. And the necessary phase delay for POVM can be found as $\delta_{i_0} = \delta + \pi/2$ from Eq. (E13).

Spatial resolution of two-point sources. Recently, the spatial resolution of two equally bright strong point sources was studied in [35] by considering the sources aligned parallel to the two-mode interferometer.

In this section, we consider a similar model with two circular disk sources on the surface of the source plane at locations $\mathbf{r}_1 = (x_1, y_1, R)$ and $\mathbf{r_2} = (x_2, y_2, R)$ but with different effective temperatures T_1 and T_2, and same sizes a. We assume that in the far field $\{x_i, y_i\} \ll R$ and $a \ll R$. We analyze two cases: when the sources are aligned or not aligned with the two antennas. For two circular sources with equal size, the temperature distribution over the surface can be written as

$$T_{\mathrm{eff}}(x, y) = \sum_{i=\{1,2\}} T_i \mathrm{circ}(x - x_i, y - y_i). \tag{65}$$

Then we can define the four parameters that we want to estimate as source separation ($s_x = x_1 - x_2$), ($s_y = y_1 - y_2$) and centroid of the two sources [$t_x = (x_1 + x_2)/2$], [$t_y = (y_1 + y_2)/2$]. In Appendix F, we express the QFI matrix elements for all four parameters. Since these equations are quite complicated, we check the important limits. Since we want to resolve the two-point sources even for very small separation, we check the limit $s_x, s_y \to 0$. Then we have QFI matrix elements for estimating the source separation as $\mathscr{F}_{s_i} \to 4\pi^2 v_i^2 \eta \kappa T$ and $\mathscr{F}_{s_x s_y} \to 4\pi^2 v_x v_y \eta \kappa T$, if $T_1 = T_2 = T$.

If we assume two sources aligned parallel to the two-mode interferometer [$y_1 = 0, y_2 = 0$ and $\varphi = 0 \to v = v_x = \Delta r/(R\lambda)$ and $s_x \to s, \quad t_x \to t$] we can simplify our problem to a single dimension. We show the dependence of the QFI matrix elements on average temperature [$T = (T_1 + T_2)/2$] and temperature difference $\Delta T = T_1 - T_2$ assuming $T_1 \geqslant T_2$. In Fig. 4(a), we plot $\mathscr{F}_s$ with respect to source separation s for different average temperatures. As expected, when the temperature increases, the QFI for estimating the separation also increases. For $T = 300$ K and $\Delta r = 4$ m, we have a QFI around 0.027 $1/\mathrm{km}^2$ which corresponds to a standard deviation of 6 km for only two receivers for the separation estimation. In Fig. 4(b), we see that, as we increase the temperature difference between the two-point sources, the QFI becomes less oscillatory and at $\Delta T \to 2T$, the oscillatory behavior disappears. In the limit $\Delta T \to 2T$, or $s \to 0$ the QFI for estimating s becomes

$$\mathscr{F}_s \to 4\pi^2 v^2 \eta \kappa T, \tag{66}$$

which is the limit given by the solid black line in Fig. 4(b). We calculated the CFI from heterodyne detection to estimate the source separation in Eq. (F14). If the size of the sources is very small and in the limit $\eta\kappa T \ll 1$ the CFI for estimating the source separation simplifies to

$$F_{s_i} \xrightarrow{\eta\kappa T \ll 1} 8\pi^2 \eta^2 \kappa^2 T^2 v_i^2 \sin^2[\pi(s_x v_x + s_y v_y)]. \tag{67}$$

When the source separation goes to zero ($s_x, s_y \to 0$), F_{s_i} tends to zero. We compare the QFI with CFI in Eq. (F14) from heterodyne detection in Fig. 4(c). As we can see, the CFI goes to zero for small source separation. Therefore, we can conclude that Rayleigh's curse limits heterodyne detection. The POVM from the SLD eliminates that limitation. We give the elements of the matrix $\mathbf{M}_s$, g_s^1, and g_s^2 in Appendix F. The phase difference for combining two spatial modes of the interferometer can be found as $\delta_s = 2\pi(t_x v_x + t_y v_y) - \pi$. Assuming the alignment of the spatial mode separation parallel to source separation, it becomes $\delta_s = 2\pi t v - \pi$.

The QFI matrix elements for estimating the centroid is given in Eq. (F6). We assume that the two sources aligned again parallel to two spatial modes of the interferometer [$y_1 = 0, \ y_2 = 0$ and $\varphi = 0 \to v = v_x = \Delta r/(R\lambda)$ and $s_x \to s, \quad t_x \to t$] and $\mathscr{F}_{t_x, t_x} \to \mathscr{F}_t$. In Fig. 4(d), we see that the $\mathscr{F}_t$ increases when we increase the temperature. For $T = 300$ K and $\Delta r = 4$ m, we have a QFI $\mathscr{F}_t \sim 0.11$ $1/\mathrm{km}^2$ which corresponds to a standard deviation of 3 km for estimating the centroid. When $sv \sim 0.5$, $\mathscr{F}_t$ goes to zero for equally bright sources. In Fig. 4(e) we see that it is not zero for $sv \sim 0.5$, if $\Delta T \neq 0$, and the oscillation of $\mathscr{F}_t$ decreases when we increase the temperature difference. In the limit $s \to 0$, $\mathscr{F}_t$ simplifies to

$$\mathscr{F}_t \to 32\pi^2 v^2 \eta \kappa T \tag{68}$$

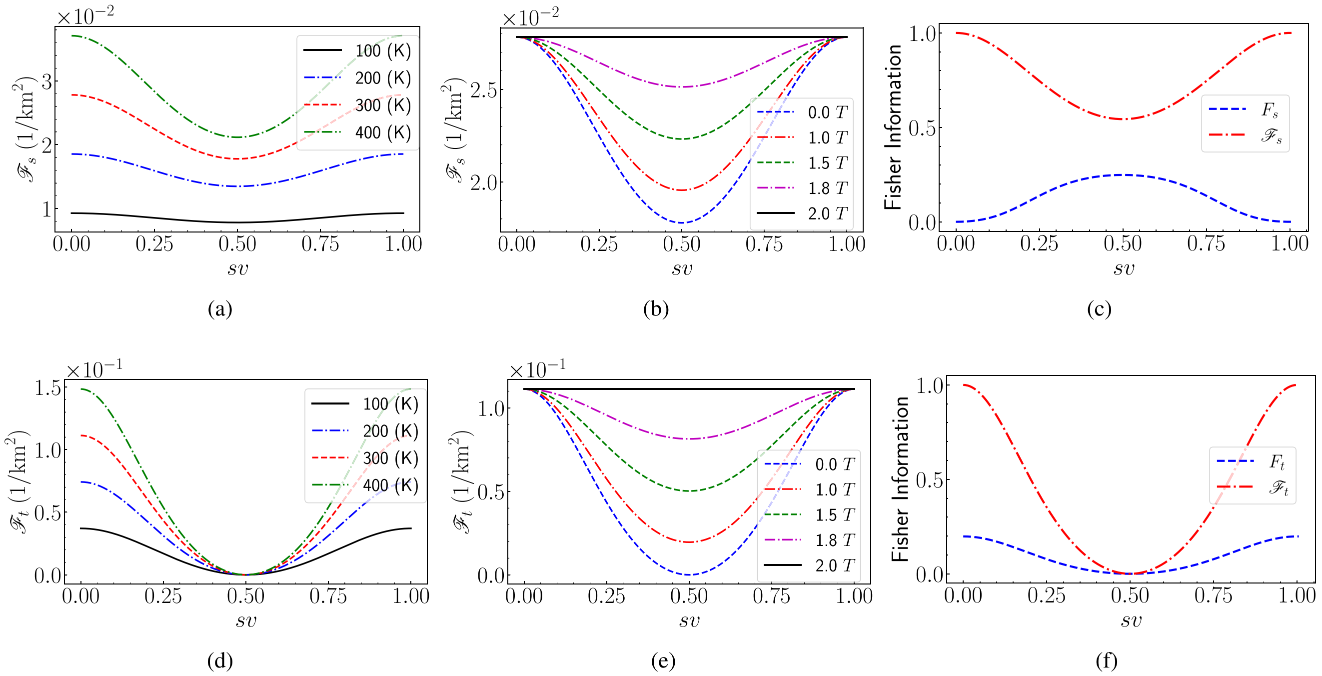

FIG. 4. (a) The QFI $\mathscr{F}_s$ of estimating the separation of two-point sources as a function of source separation s for different average temperatures with $\Delta T = 0$ and $\Delta r = 4$ m. (b) The QFI $\mathscr{F}_s$ with respect to s for various temperature differences ΔT for $T = 300$ K. (c) The QFI $\mathscr{F}_s$ (red dotted-dashed) and CFI for heterodyne detection (blue dashed) for estimating the separation of two-point sources with same temperatures T as a function of s. Both the QFI and the CFI scaled by $4\pi^2 v^2 \eta\kappa T$. (d) The QFI $\mathscr{F}_t$ respect to s for different average temperature T. (e) The QFI $\mathscr{F}_t$ respect to s for various temperature difference ΔT for $T = 300$ K. (f) The QFI $\mathscr{F}_t$ (red dotted-dashed) and CFI for heterodyne detection F_t (blue dashed) for estimating the centroid of two-point sources with same temperatures T as a function of s (both the QFI and the CFI scaled by $32\pi^2 v^2 \eta\kappa T$). For (a), (b), (d), and (e), v is fixed by taking the separation Δr of the two antennas 4 m and we have $\eta \sim 10^{-4}$. The curves are ordered by increasing value of the QFI from solid black to green dotted-dashed lines in (a) and (d), and from blue dashed to solid black lines in (b) and (d).

for $\Delta T = 0$. The CFI for heterodyne detection is given in Eq. (F13). For small sources we consider again the limit $\eta\kappa T \ll 1$, and we ignore the higher-order terms of $\eta\kappa T$. Then we have

$$F_{t_i} \xrightarrow{\eta\kappa T \ll 1} 32\pi^2\eta^2\kappa^2 T^2 {v_i}^2 \cos^2[\pi(s_x v_x + s_x v_y)]. \qquad (69)$$

If the source separation goes to zero ($s_x, s_y \to 0$), we still have a finite F_{t_i}, unlike the CFI for source separation. In Fig. 4(f), we compare $\mathscr{F}_t$ with F_{t_i}. When the source separation goes to zero, both Fisher information goes to a constant, and both go to zero at $sv \to 0.5$. However, the QFI is five times larger than the CFI from heterodyne detection. Again the phase difference for the POVM from the SLD can be found as $\delta_t = 2\pi t v + \pi/2$.

Both QFIs, for source separation and centroid, are periodic functions with a period of $1/v$ in the case of two point sources (see Ref. [35]). The information on the position of the sources is only encoded in phases. The QFIs are maximum at $s = 0$ or at $s = 1/v = \lambda R/\Delta r$. The fact that $sv = \frac{1}{2}$ the QFI has a minimum (or even vanishes for the centroid estimation) has its origin in destructive interference. For this value of sv, the two waves from the centroid position to the two receivers have a phase difference of π that makes that the off-diagonal matrix element in the correlation matrix $\langle \hat{b}_i^\dagger \hat{b}_j \rangle$ vanish. Hence, the QFI has to drop from the finite value at $sv = 0$ to this minimum.

C. 1D *n*-mode interferometer arrays

The previous section considered a two-mode interferometer for analytical calculations and compared the QFI with its POVM and CFI for heterodyne detection. To compare our results with SMOS, we extend the two-mode interferometer to a 1D array of n single-mode receivers. We investigate numerically how the QFI changes when increasing the number n of interferometer modes. We assume the antenna array aligned with the x axis on the detection plane and denote the maximum baseline separation of the two most distant antennas by $\Delta r_{\max}$.

Resolution of two-point sources for n-mode interferometer array. We assume that both sources have the same sizes and temperatures ($\Delta T = 0$ and $T_1 = T_2 = T$) and that they are parallel to the antenna array. In Fig. 5(a), we see that when we increase the number of receivers, the behavior of $\mathcal{F}_s$ changes. It is still oscillatory as a function of sv with a period of 2π. However, for each oscillation, we have $n - 2$ additional maxima. Moreover, in Fig. 5(b), we see that $\mathcal{F}_s$ increases gradually when we increase the number of receivers and the maximum baseline increases as $\Delta r_{\max} = (n-1)\Delta r$. For $\Delta r = 1$ m and $T = 300$ K, the standard deviation for estimating the source separation is ~23 km for the two-mode interferometer. For the 20-mode interferometer, we find a standard deviation of around 0.65 km. Further, if we keep the baseline fixed as 4 m, the QFI increases linearly with the number of receivers, as we

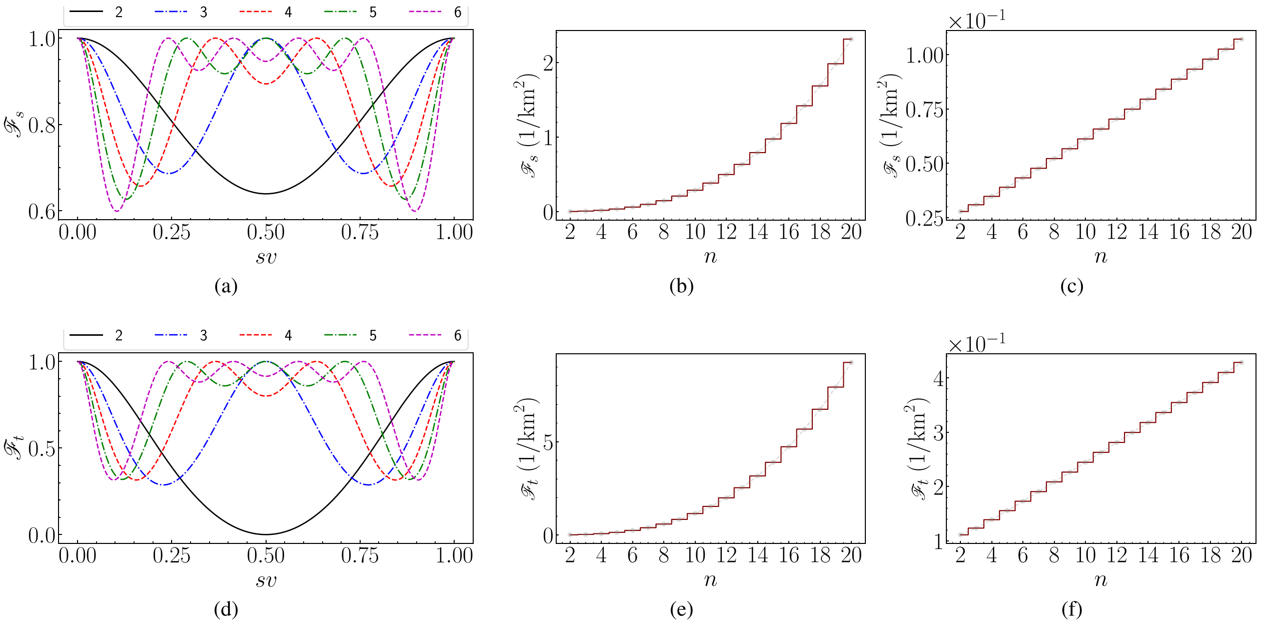

(a) (b) (c)

(d) (e) (f)

FIG. 5. (a) The QFI $\mathscr{F}_s$ as a function of s for 2,3,4,5,6 mode interferometers and each curve is scaled by its maximum values which are $\sim 1.7 \times 10^{-3}$, $\sim 6.9 \times 10^{-3}$, $\sim 17.3 \times 10^{-3}$, $\sim 34.7 \times 10^{-3}$, $\sim 60.8 \times 10^{-3}$ 1/km^2, respectively. (b) The QFI $\mathscr{F}_s$ with respect to a number of interferometer modes n. (c) The QFI $\mathscr{F}_s$ with respect to a number of interferometer modes n. (d) The QFI $\mathscr{F}_t$ as a function of s for 2,3,4,5,6 mode interferometers. Each curve is scaled by its maximum values which are $\sim 0.67 \times 10^{-2}$, $\sim 2.78 \times 10^{-2}$, $\sim 6.96 \times 10^{-2}$, $\sim 13.9 \times 10^{-2}$, $\sim 24.3 \times 10^{-2}$ 1/km^2, respectively. (e) The QFI $\mathscr{F}_t$ with respect to a number of interferometer modes n. [For all, the separation of two nearest antenna Δr is 1 m, and $\eta \sim 10^{-4}$. The maximum baseline is $\Delta r_{\max} = (n-1)\Delta r$.)] (f) The QFI $\mathscr{F}_t$ with respect to a number of interferometer modes n. For both (c) and (f), the maximum baseline is fixed by $\Delta r_{\max} = 4$ m, in this case, separation of two nearest antenna is $\Delta r = \Delta r_{\max}/(n-1)$, and $\eta \sim 10^{-4}$. The curves are ordered by increasing value of the modes (n) from two-mode interferometer (solid black) to six-mode interferometer (purple dotted-dashed) in (a) and (d).

can see in Fig. 5(c). In this case, for a two-mode interferometer, we have a standard deviation of around 6 km, and for a 20-mode interferometer, we have 3 km.

We also checked the centroid estimation for the n-mode interferometer. It leads to similar results as for source separation. From Fig. 5(d) we see that for $sv = 0.5$ the centroid uncertainty for the two-mode interferometer diverges ($\mathscr{F}_t \sim 0$ at $sv \sim 0.5$). This is no longer the case for the array of n receivers. In Fig. 5(e), we see that $\mathscr{F}_t$ also increases with the number of modes. For the two modes, the standard deviation for estimating the centroid was $\sim$12 km. For the 20 modes, we have a standard deviation of around 0.32 km considering $\Delta r = 1$ m and $\Delta r_{\max} = (n-1)\Delta r$ for average temperature $T = 300$ K. If we keep the baseline fixed, as we can see from the Fig. 5(f), $\mathscr{F}_t$ increases linearly by n. By fixing the $\Delta r_{\max} = 4$ m, we have a standard deviation of $\sim$3 km for the two-mode interferometer; for 20 modes we have a standard deviation of $\sim$1.5 km. Thus, instead of sampling the state in time, we can increase the number of receivers to increase the QFI, and both methods can be combined as well.

Spatial resolution of single circular source for n-mode interferometer array. To analyze the effect of n for source size estimation, we consider a single circular source as given in Eq. (46). In Fig. 6, we show how the QFI for estimating a changes with n. For $a \rightarrow 0$, $\mathscr{F}_a$ increases linearly with n. We have $\mathscr{F}_a \sim 6.16 \times 10^{-2}$ 1/km^2 for single receiver which corresponds to a standard deviation of 4 km and for higher n, we have approximately $\mathscr{F}_a \propto n$ for small values of a. If we have an array of 20 antennas, $\mathscr{F}_a \sim 1.23$ 1/km^2 which gives a standard deviation of 0.9 km for estimating a. When we increase the source size a, we see that there is extra information coming from the phase differences as given by the solid lines for $\Delta r_{\max} = 6$ m and dashed lines for $\Delta r_{\max} = 4$ m. One can also see that as expected the dotted lines, corresponding to the limit $\Delta r_{\max} \rightarrow 0$, get close to the solid black line, which corresponds to a single receiver, for large values of a.

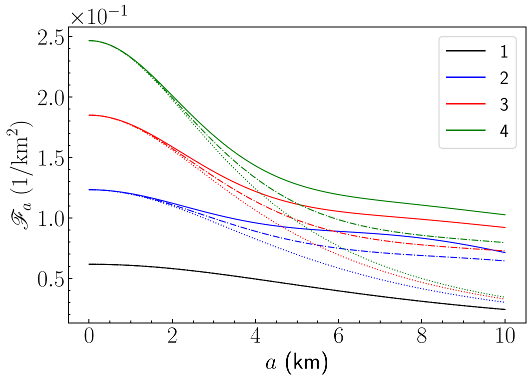

FIG. 6. The QFI $\mathscr{F}_a$ as a function of a for 1,2,3,4 mode interferometers, which are given by black (the lowest single) curve, blue, red, and green (the top) curves, respectively. The maximum baseline difference is given by $\Delta r_{\max} \rightarrow 0$ for dotted lines, $\Delta r_{\max} = 4$ m for dashed lines, and $\Delta r_{\max} = 6$ m for solid lines. The black solid line corresponds to single receiver and $T = 300$ K.

As a mathematical limit, we can take $\Delta r_{\max} \to 0$. Then the additional information from phase differences of a receiver pair will vanish [see Figs. 2(a) and 3(a)]. One can also compare the QFI in Eq. (48) for a single mode with the QFI in Eq. (59) for a two-mode receiver. In the limit $a \to 0$, we see that the QFI for estimating a is doubled. Yet, the FI for estimating a from heterodyne detection in Eqs. (50) and (60) always vanishes in this limit $a \to 0$. In Fig. 6, the QFI to estimate a linearly increases with n. But the FI from heterodyne detection is zero for the small source sizes in the limit $a \to 0$ even for $n \to \infty$. Thus, we see that resolution is limited for heterodyne detection for small source sizes. To get the quantum super-resolution for estimating the image, one needs to linearly combine the modes $\hat{b}_i$ of the n-mode interferometer. For that aim, one needs to calculate the elements of the matrix $\mathbf{M}_i$ numerically. Each normalized eigenvector of $\mathbf{M}_i$ maps to a set of operators $\bar{\mathbf{d}}$ by linear combination of the operators in $\bar{\mathbf{b}}$ with corresponding weights and phases. One can design a setup using these weights and phases in the eigenvectors to achieve the resolutions for a chosen parameter given in this section.

IV. CONCLUSION

In summary, we studied possible quantum advantages in passive microwave remote sensing. Starting from a microscopic current density distribution in the source plane corresponding to a position-dependent brightness temperature $T_{\text{eff}}(x, y)$, we derived the general partially coherent state received by an array of antennas. From the dependence of that partially coherent states on parameters that characterize the sources, such as the radius a and brightness temperature T of a uniform circular source, we obtained the QFI and hence the QCRB for the smallest possible uncertainty with which these parameters can be estimated based on measurements of the multimode state of the antennas. We showed how the optimal measurements allowing one to estimate a single parameter can be obtained for a general array interferometer with antennas placed at arbitrary positions. In general, the optimal measurements correspond to photon-detection in certain detector modes that can be obtained from the original receiver modes by mode mixing via beam splitters and phase shifters. For single-mode and two-mode interferometers, we gave explicit analytical results for the best possible resolution of one or two uniform circular sources, both in a and T and demonstrated a clear quantum advantage over the classical strategy corresponding to direct heterodyne measurements of the receiver modes. In the limit of small source sizes, we recover known results for the measurement of the centroid and separation of two-point sources. We benchmarked our results with the performance of the SMOS mission, which achieves about 35-km resolution with 69 antennas deployed on three 4-m long arms arranged in a Y shape, operating at 21 cm the wavelength, and flying at a height of 758 km above Earth. As an example, we showed that by using the optimal measurements, a single arm of length 4 m with 20 antennas and a single measurement would allow a spatial resolution of about 1.5 km. With a smaller satellite, a more than 20-fold increase of resolution compared to SMOS could be achieved. By increasing the size of the array to 19 m, the 20 antennas should give rise to a spatial resolution down to 300 m. Substantially better resolutions can be achieved if we allow more measurements. If we assume that the number of samples is given by the time the satellite flies over the object whose size one wants to estimate divided by the inverse bandwidth, even with a single receiver a spatial resolution down to a few meters and a radiometric resolution of a fraction of a Kelvin become possible in principle.

Our results generalize previous approaches to quantum-enhanced imaging based typically on weak sources (photon numbers on average smaller than 1 per mode) or point sources, and pave the way to quantum metrological sensitivity enhancements in real-world scenarios in passive microwave remote sensing. Several challenges remain. Experimentally, single-photon detection in the microwave regime is still difficult but starts to become available [82], and even number-resolved photon detection in the microwave regime has meanwhile been demonstrated [83]. It requires very low temperatures for operating superconducting qubits that would have to be maintained on a long timescale on the satellite. From the theoretical side, an extension to a many-parameter regime requiring adaption of the optimal measurements will be crucial for true imaging. Post-measurement beam synthesis that is common in interferometric astronomy does not work here, as already the detection modes depend on the pixel in the image that one wants to focus on. Nevertheless, the substantial quantum advantages demonstrated here theoretically in a relatively simple but real-world scenario give hope that quantum metrology can help to significantly improve the resolution of passive Earth observation schemes, with corresponding positive impact on the data available for feeding climate models, weather forecasts, and forecasts of floodings.

ACKNOWLEDGMENTS

D.B. and E.K. are grateful for support by the DFG, Project No. BR 5221/3-1. D.B. thanks Y. Kerr, B. Rougé, and the entire SMOS team in Toulouse for valuable insights into that mission.

APPENDIX A: BRIGHTNESS TEMPERATURE AND CURRENT DENSITY FLUCTUATIONS

The number of photons that pass through a certain antenna area A_D in a certain time t_D can be found from $\bar{n} = A_D t_D \Phi$, where Φ is the photon flux. For a given intensity I, the photon flux for frequency ω_0 can be found by $\Phi = I/(\hbar\omega_0)$. If the total energy density on the antenna is U_D, then the intensity can be written as $I = U_D c$. Then $\bar{n}$ becomes $\bar{n} = A_D t_D U_D c/(\hbar\omega_0)$. In the microwave regime $\hbar\omega \ll k_B T$, the energy density (energy per unit volume per frequency) from black-body radiation at frequency ω with a temperature distribution $T(x,y)$ on the surface of radiation at the ith antenna position is given by [43]

$$u_D(\omega) = \frac{k_B}{2\pi^3 c^3}\int dx\,dy\,\omega^2 \frac{T_B(x,y)\cos\tilde{\theta}(x,y)}{|\mathbf{r}-\mathbf{r}_i|^2}, \tag{A1}$$

where the brightness temperature is defined as $T_B(x,y) \equiv T(x,y)B(x,y;\omega,\tilde{\theta},\tilde{\varphi})$. Earth is rather a gray than a black body, therefore, the emissivity $B(x,y;\omega,\tilde{\theta},\tilde{\varphi})$ of the patch in the direction of the satellite given by polar and azimuthal angles is introduced. One can take the integral over ω using the filter function in Eq. (21) to find the total energy density (energy per volume) and it becomes

$$U_D = \frac{k_B\omega_0^2 B}{2\pi^3 c^3}\int dx\,dy \frac{T_B(x,y)\cos\tilde{\theta}(x,y)}{|\mathbf{r}-\mathbf{r}_i|^2}. \tag{A2}$$

Then the photon number on the receiver becomes

$$\bar{n} = \frac{2k_B}{\pi\hbar\omega_0}\left(\frac{A_D}{\lambda^2}\right)(t_D B)\int dx\,dy \frac{T_B(x,y)\cos\tilde{\theta}(x,y)}{|\mathbf{r}-\mathbf{r}_i|^2}. \tag{A3}$$

For simplicity of the receivers scattering function, we set $A_D \sim \lambda^2$ and $t_D \sim 1/B$. Comparing Eq. (A3) with (29), we define $\langle|\tilde{j}_{t,i}(\mathbf{r},\omega)|^2\rangle \equiv K_1 T_{\mathrm{B}}(x,y)\cos\tilde{\theta}(x,y)\delta(z-R)$ with a constant $K_1 = 32\tau_c k_B/(3l_c^3\mu_0 c)$ which agrees with the result in Ref. [43].

APPENDIX B: COMMUTATION RELATIONS OF SLD'S FOR *n*-MODE INTERFEROMETER

The SLD for the ith parameter is given in Eq. (38) for the n-mode interferometer. To find the $[\mathscr{L}_i, \mathscr{L}_j]$ we write

$$\mathscr{A}_i = \sum_j^n g_i^j \hat{b}_j^\dagger \hat{b}_j, \quad \mathscr{B}_i = \sum_{j<k}^n \left[g_i^{jk}\hat{b}_j^\dagger\hat{b}_k + \left(g_i^{jk}\right)^* \hat{b}_k^\dagger \hat{b}_j\right]. \tag{B1}$$

Using $[\hat{b}_l, \hat{b}_k^\dagger] = \delta_{kl}$, one can write $\hat{b}_k^\dagger\hat{b}_l\hat{b}_m^\dagger\hat{b}_p = \hat{b}_m^\dagger\hat{b}_p\hat{b}_k^\dagger\hat{b}_l + \hat{b}_k^\dagger\hat{b}_p\delta_{lm} - \hat{b}_m^\dagger\hat{b}_l\delta_{kp}$. Then, we find the rest of the commutation relations as follows:

$$[\mathscr{A}_i, \mathscr{A}_j] = \sum_{kl}^n g_i^k g_j^l (\hat{b}_l^\dagger\hat{b}_k\delta_{kl} - \hat{b}_k^\dagger\hat{b}_l\delta_{kl}) = 0, \tag{B2}$$

$$[\mathscr{A}_i, \mathscr{B}_j] = \sum_{l<m}^n \left[\left(g_i^l - g_i^m\right)g_j^{lm}\hat{b}_l^\dagger\hat{b}_m + \left(g_i^m - g_i^l\right)\left(g_j^{lm}\right)^*\hat{b}_m^\dagger\hat{b}_l\right], \tag{B3}$$

$$[\mathscr{B}_i, \mathscr{A}_j] = -\sum_{l<m}^n \left[\left(g_j^l - g_j^m\right)g_i^{lm}\hat{b}_l^\dagger\hat{b}_m + \left(g_j^m - g_j^l\right)\left(g_i^{lm}\right)^*\hat{b}_m^\dagger\hat{b}_l\right], \tag{B4}$$

$$\begin{aligned}[\mathscr{B}_i, \mathscr{B}_j] = &\sum_{k<l<m}^n \left(g_i^{kl}g_j^{lm} - g_i^{lm}g_j^{kl}\right)b_k^\dagger b_m + \left[\left(g_i^{lm}\right)^*\left(g_j^{kl}\right)^* - \left(g_i^{kl}\right)^*\left(g_j^{lm}\right)^*\right]b_m^\dagger b_k \\ &+ \sum_{k<\min(l,p)}^n \left[\left(g_i^{kl}\right)^* g_j^{kp}\hat{b}_l^\dagger\hat{b}_p - g_i^{kl}\left(g_j^{kp}\right)^*\hat{b}_p^\dagger\hat{b}_l\right] + \sum_{\{k,m\}<l}^n \left[g_i^{kl}\left(g_j^{ml}\right)^*\hat{b}_k^\dagger\hat{b}_m - \left(g_i^{kl}\right)^* g_j^{ml}\hat{b}_m^\dagger\hat{b}_k\right],\end{aligned} \tag{B5}$$

where $\sum_{k<\min(l,p)}^n \equiv \sum_l^n\sum_p^n\sum_k^{\min(l,p)-1}$ and $\sum_{\{k,m\}<l}^n \equiv \sum_l^n\sum_m^{l-1}\sum_k^{l-1}$. For the two-mode interferometer ($n=2$), the diagonal elements of $\mathbf{M}_i$ are the same for any parameter estimation due to the central symmetry of two antenna. Then, we have $[\mathscr{A}_i, \mathscr{B}_j] = [\mathscr{B}_i, \mathscr{A}_j] = 0$, the first summation vanishes, and we have $[\mathscr{B}_i, \mathscr{B}_j] = [g_i^{12}(g_j^{12})^* - (g_i^{12})^* g_j^{12}](\hat{b}_1^\dagger b_1 - \hat{b}_2^\dagger\hat{b}_2)$. Since $\langle b_1^\dagger b_1\rangle = \langle b_2^\dagger b_2\rangle = \bar{n}$, we obtain $\mathrm{Tr}\,[\rho_{\mathrm{int}}[\mathscr{L}_i, \mathscr{L}_j]] = 0$.

APPENDIX C: GENERAL QFI AND THE ELEMENTS OF THE MATRIX M FOR A TWO-MODE INTERFEROMETER

In this Appendix, we give the general results for the elements of the QFI and the matrix $\mathbf{M}_i$ for a two-mode interferometer, assuming that all the elements of the covariance matrix depend on the parameter μ_i that we want to estimate. Using the covariance matrix for a two-mode interferometer one finds the QFI matrix elements as

$$\begin{aligned}\mathscr{F}_{ij} = \frac{8}{\mathscr{D}}\big\{&\partial_i\xi^*\partial_j\xi[(1-4\chi^2)^2 - 4(1+4\chi^2)|\xi|^2] + \partial_i\xi\partial_j\xi^*[(1-4\chi^2)^2 - 4(1+4\chi^2)|\xi|^2] \\ &+ 4\xi\partial_i\xi^*[\xi\partial_j\xi^*(1+4\chi^2-4|\xi|^2) + 2\chi\partial_j\chi(1-4\chi^2+4|\xi|^2)] + 4\xi^*\partial_i\xi[\xi\partial_j\xi^*(1+4\chi^2-4|\xi|^2) \\ &+ 2\chi\partial_j\chi(1-4\chi^2+4|\xi|^2)] + 2\partial_i\chi(-1+4\chi^2-4|\xi|^2)[-4\chi(\xi\partial_j\xi^* + \xi^*\partial_j\xi) + \partial_j\chi(-1+4\chi^2+4|\xi|^2)]\big\},\end{aligned} \tag{C1}$$

where the denominator is given by

$$\mathscr{D} = (-1 + 4\chi^2 - 4|\xi|^2)[16\chi^4 + (1 - 4|\xi|^2)^2 - 8\chi^2(1 + |\xi|^2)]. \tag{C2}$$

Using the SLD given in Eq. (38) we find the diagonal elements of the matrix $\mathbf{M}_i$ given in Eq. (56) as

$$g_i^1 = \frac{2(4\partial_i\chi|\xi|^2 + 4\partial_i\chi\chi^2 - 4\partial_i\xi\xi^*\chi - 4\partial_i\xi^*\xi\chi - \partial_i\chi)}{16\chi^4 - 8\chi^2(4|\xi|^2 + 1) + (1 - 4|\xi|^2)^2}, \tag{C3}$$

where the two diagonal elements are the same due to the symmetry with respect to the center of the two antennas, and

$$g_i^2 = \frac{2}{\mathscr{D}}\{-\partial_i\xi(16|\xi|^2\chi^2 + 4|\xi|^2 - 16\chi^4 + 8\chi^2 - 1) - \partial_i\xi^*[4\xi^2(4|\xi|^2 - 1) - 16\xi^2\chi^2] - \partial_i\chi[32\xi\chi^3 - 8\xi\chi(4|\xi|^2 + 1)]\}, \tag{C4}$$

where $\mathscr{D}$ is given in Eq. (C2).

APPENDIX D: POVM FOR HETERODYNE DETECTION

The POVM for heterodyne detection is given in Ref. [34], and the CFI analyzed for the weak thermal sources. Here we briefly introduce the POVM for heterodyne detection. Then, we compare our results for the QFI with the CFI for heterodyne detection. The POVM is given as

$$E(\nu_1, \nu_2) = \frac{1}{\pi^2}|\nu_1, \nu_2\rangle\langle\nu_1, \nu_2|, \tag{D1}$$

where $|\nu_1, \nu_2\rangle$ is a coherent state with normalization given by $\int d^2\nu_1 d^2\nu_2 E(\nu_1, \nu_2) = \mathbb{1}$. The covariance matrix for a two-mode interferometer is given in Eq. (55). Using the corresponding state for the two-mode interferometer we can find the observation probability for any parameter μ_i, in terms of the elements of the covariance matrix as

$$P(\nu_1, \nu_2|\mu_i) = \frac{1}{\pi^2[(1 + \bar{n})^2 - |\xi|^2]} \exp\left[\frac{(-|\nu_1|^2 - |\nu_2|^2)(1 + \bar{n}) + \xi\nu_1^*\nu_2 + \xi^*\nu_2^*\nu_1}{(1 + \bar{n})^2 - |\xi|^2}\right]. \tag{D2}$$

The Fisher information for the parameter μ_i can be found as

$$\begin{aligned} F_i &= \int d^2\nu_1 d^2\nu_2 \frac{1}{P(\nu_1, \nu_2|\mu_i)}\left(\frac{\partial P(\nu_1, \nu_2|\mu_i)}{\partial\mu_i}\right)^2 \\ &= \int d^2\nu_1 d^2\nu_2 P(\nu_1, \nu_2|\mu_i) f(\nu_1, \nu_2) \\ &= \langle f(\nu_1, \nu_2)\rangle, \end{aligned} \tag{D3}$$

where $f(\nu_1, \nu_2)$ is a polynomial function of second- and fourth-order correlations of ν_1 and ν_2, defined as

$$f(\nu_1, \nu_2) \equiv \{\partial_{\mu_i} \ln [P(\nu_1, \nu_2|\mu_i)]\}^2 = \frac{1}{[P(\nu_1, \nu_2|\mu_i)]^2}\left(\frac{\partial P(\nu_1, \nu_2|\mu_i)}{\partial\mu_i}\right)^2. \tag{D4}$$

With Wick's theorem for Gaussian states, the fourth-order statistic can be written as

$$\langle x_1x_2x_3x_4\rangle = \langle x_1x_2\rangle\,\langle x_3x_4\rangle + \langle x_1x_3\rangle\,\langle x_2x_4\rangle + \langle x_1x_4\rangle\,\langle x_2x_3\rangle, \tag{D5}$$

where $x_i \in \{\nu_1, \nu_1^*, \nu_2, \nu_2^*\}$. We can also write $\langle|\nu_1|^2\rangle = \langle|\nu_2|^2\rangle = 1 + \bar{n}$ and $\langle\nu_1^*\nu_2\rangle = \xi$, $\langle\nu_2^*\nu_1\rangle = \xi^*$.

APPENDIX E: UNIFORM CIRCULAR SOURCE FOR A TWO-MODE INTERFEROMETER

We find the elements of the covariance matrix describing the state of two-mode interferometers in Eq. (55). Then for a circular source with size a located at position (x_0, y_0, R) with the assumption $x_0, y_0 \ll R$ in the source plane we have

$$\begin{aligned} \bar{n} &= \frac{\kappa T}{R^2}\int dx\,dy\,\mathrm{circ}(x - x_0, y - y_0) \\ &= \frac{\pi a^2\kappa T}{R^2}, \end{aligned} \tag{E1}$$

and χ and ξ become

$$\chi = \frac{1}{2} + \frac{\pi a^2 \kappa T}{R^2}, \tag{E2}$$

$$\begin{aligned} \xi = \langle b_2^\dagger b_1 \rangle &= \frac{\kappa T}{R^2} \int dx\, dy\, \mathrm{circ}(x - x_0, y - y_0) \exp\left[2\pi i (x v_x + y v_y)\right] \\ &= \frac{\kappa T a^2}{R^2} \frac{J_1\left(2\pi a \sqrt{v_x^2 + v_y^2}\right)}{a\sqrt{v_x^2 + v_y^2}} \exp\left[2\pi i (x_0 v_x + y_0 v_y)\right], \end{aligned} \tag{E3}$$

where $v_x = \Delta r \cos\varphi/(\lambda R)$, $v_y = \Delta r \sin\varphi/(\lambda R)$, with $\mathbf{\Delta r} = \Delta r(\cos\varphi, \sin\varphi, 0)$. Note that $\sqrt{v_x^2 + v_y^2} = \Delta r/(\lambda R)$.

1. Quantum Fisher information: The uniform circular source

We found the QFI for estimating a is as

$$\mathscr{F}_a = \frac{8\pi^2 a \Delta r^2 \kappa T}{\mathscr{D}_a}\left[\pi a \Delta r^2 (\pi a^2 \kappa T + R^2)(J_0^2 + 1) - 2\Delta r \lambda R (2\pi a^2 \kappa T + R^2) J_0 J_1 + a\kappa \lambda^2 R^2 T (J_0^2 + 1) J_1^2\right], \tag{E4}$$

where

$$\mathscr{D}_a = \left(\pi^2 a^2 \Delta r^2 - \lambda^2 R^2 J_1^2\right)\left[\Delta r^2 (\pi a^2 \kappa T + R^2)^2 - \kappa^2 \lambda^2 R^2 T^2 J_1^2\right], \tag{E5}$$

and $J_i(\frac{2a\Delta r\pi}{R\lambda})$ are the Bessel functions of the first kind and ith order. The QFI for estimating T becomes

$$\mathscr{F}_T = \frac{2\kappa a^2\left[\pi \Delta r^2 (\pi a^2 \kappa T + R^2) - \kappa \lambda^2 R^2 T J_1^2\right]}{T\left[\Delta r^2 (\pi a^2 \kappa T + R^2)^2 - a^2 \kappa^2 \lambda^2 R^2 T^2 J_1^2\right]}. \tag{E6}$$

The other elements regarding the source size and the temperature of the circular source can be found as

$$\mathscr{F}_{aT} = \frac{4\pi a \Delta r \kappa \left[\Delta r (\pi a^2 \kappa T + R^2) - a\kappa \lambda R T J_0 J_1\right]}{\Delta r^2 (\pi a^2 \kappa T + R^2)^2 - a^2 \kappa^2 \lambda^2 R^2 T^2 {J_1}^2}. \tag{E7}$$

The QFI matrix elements for estimating the source locations can be written as

$$\mathscr{F}_{i_0 j_0} = \frac{8\pi^2 R^2 \lambda^2 \kappa T {J_1}^2 v_i v_j}{\pi \Delta r^2 (\pi a^2 \kappa T + R^2) - \kappa \lambda^2 R^2 T {J_1}^2}, \tag{E8}$$

where $i, j \in \{x, y\}$.

2. Elements of the matrix $\mathbf{M}_i$ for a two-mode interferometer: The uniform circular source

To combine two modes of the receivers for the optimum measurements, we calculate δ as given in Eq. (57). We find the matrix elements of $\mathbf{M}_a$ as

$$g_a^1 = \frac{2\pi \Delta r^2 R^2}{\mathscr{D}_a}\{\pi a \Delta r^2 (\pi a^2 \kappa T + R^2) + \lambda R J_1 [a\kappa \lambda R T J_1 - \Delta r (2\pi a^2 \kappa T + R^2) J_0]\}, \tag{E9}$$

$$g_a^2 = \frac{2\pi \Delta r^2 R^2}{\mathscr{D}_a}\{a J_0 [\pi \Delta r^2 (\pi a^2 \kappa T + R^2) + \kappa \lambda^2 R^2 T J_1^2] - \Delta r \lambda R (2\pi a^2 \kappa T + R^2) J_1\} e^{-i\delta}, \tag{E10}$$

where $\delta = v_x x_0 + v_y y_0$. For the temperature estimation we get the elements of $\mathbf{M}_T$ as

$$g_T^1 = \frac{\Delta r^2 R^2 (\pi a^2 \kappa T + R^2)}{\Delta r^2 T (\pi a^2 \kappa T + R^2)^2 - a^2 \kappa^2 \lambda^2 R^2 T^3 J_1^2}, \tag{E11}$$

$$g_T^2 = -\frac{a \Delta r \kappa \lambda R^3 J_1 e^{-i\delta}}{a^2 \kappa^2 \lambda^2 R^2 T^2 J_1^2 - \Delta r^2 (\pi a^2 \kappa T + R^2)^2}. \tag{E12}$$

Finally, for the source location we found

$$\begin{pmatrix} g^2_{x_0} \\ g^2_{y_0} \end{pmatrix} = -\frac{2\pi\,\Delta r^2 R^2 J_1 e^{i(-\delta+\pi/2)}}{a\big[\pi\,\Delta r^2(\pi a^2\kappa T + R^2) - \kappa\lambda^2 R^2 T J_1^2\big]}\begin{pmatrix}\cos(\varphi) \\ \sin(\varphi)\end{pmatrix}, \tag{E13}$$

and $g^1_{x_0} = g^1_{y_0} = 0$.

3. Classical Fisher information for heterodyne detection: The uniform circular source

Since we calculated the elements of the covariance matrix in Eqs. (E1) and (E2) we can calculate Eqs. (D2) and (D4). Using the CFI for the heterodyne detection in Eq. (D3), we can write the result for estimating the source size as

$$\begin{aligned} F_a = {}& \frac{8\pi^2 a^2\kappa^2 T^2\Delta r^3(\pi a^2\kappa T + R^2)}{D_a}\big[4a^5\kappa^5\lambda^5 R^5 T^5 J_0 {J_1}^5 - 2a^2\Delta r^3\kappa^2\lambda^2 R^2 T^2(\pi a^2\kappa T + R^2)^3({J_0}^2 + 1)J_1^2 \\ & + \Delta r^5(\pi a^2\kappa T + R^2)^5({J_0}^2 + 1) - 4a\Delta r^4\kappa\lambda R T(\pi a^2\kappa T + R^2)^4 J_0 J_1 \\ & - 7a^4\Delta r\kappa^4\lambda^4 R^4 T^4(\pi a^2\kappa T + R^2)({J_0}^2 + 1){J_1}^4 + 16a^3\Delta r^2\kappa^3\lambda^3 R^3 T^3(\pi a^2\kappa T + R^2)^2 J_0 J_1^3\big], \end{aligned} \tag{E14}$$

with

$$D_a = \big[\Delta r^2(\pi a^2\kappa T + R^2)^2 - a^2\kappa^2\lambda^2 R^2 T^2 J_1^2\big]^4. \tag{E15}$$

The estimation of the temperature becomes

$$\begin{aligned} F_T = {}& \frac{2a^2\Delta r^2\kappa^2(\pi a^2\kappa T + R^2)}{D_T}\big[\pi^2 a^2\Delta r^6(\pi a^2\kappa T + R^2)^5 - a^4\kappa^4\lambda^6 R^6 T^4(3\pi a^2\kappa T + 7R^2)J_1^6 \\ & + \Delta r^4\lambda^2 R^2(\pi a^2\kappa T + R^2)^3(-5\pi^2 a^4\kappa^2 T^2 - 2\pi a^2\kappa R^2 T + R^4)J_1^2 + a^2\Delta r^2\kappa^2\lambda^4 R^4 T^2(7\pi^3 a^6\kappa^3 T^3 \\ & + 19\pi^2 a^4\kappa^2 R^2 T^2 + 10\pi a^2\kappa R^4 T - 2R^6)J_1^4\big], \end{aligned} \tag{E16}$$

where

$$D_T = \big[\Delta r^2(\pi a^2\kappa T + R^2)^2 - a^2\kappa^2\lambda^2 R^2 T^2 J_1^2\big]^4. \tag{E17}$$

APPENDIX F: TWO-POINT SOURCES FOR A TWO-MODE INTERFEROMETER

The temperature distribution of two circular sources with equal size a at locations (x_1, y_1, R) and (x_2, y_2, R) is given in Eq. (65). We assume that $\{|x_i|, |y_i|, a\} \ll R$. The elements of the covariance matrix in Eq. (55) for two-point sources with different temperature can be found using Eqs. (31), (32), and (65) as

$$\begin{aligned} \chi &= \frac{1}{2} + \sum_i \frac{\pi a^2\kappa T_i}{R^2} = \frac{1}{2} + \frac{2\pi a^2\kappa T}{R^2} \\ &= \frac{1}{2} + 2\eta\kappa T, \end{aligned} \tag{F1}$$

where $\eta = \pi a^2/R^2$, and

$$\begin{aligned} \xi = \langle b_1^\dagger b_2\rangle &= \frac{\kappa\pi a^2}{R^2}\frac{2J_1\big(\frac{2\pi a\Delta r}{R\lambda}\big)}{\frac{2\pi a\Delta r}{R\lambda}}\big(T_1 e^{2\pi i(v_x x_1 + v_y y_1)} \\ &\quad + T_2 e^{2\pi i(v_x x_2 + v_y y_2)}\big) \\ &= \frac{\kappa\eta\eta_2}{2}[(2T - \Delta T)e^{2\pi i(v_x x_1 + v_y y_1)} \\ &\quad + (2T + \Delta T)e^{2\pi i(v_x x_2 + v_y y_2)}], \end{aligned} \tag{F2}$$

where the average temperature is defined as $T \equiv (T_1 + T_2)/2$, and the temperature difference of the sources as $\Delta T \equiv T_2 - T_1$ with $T_2 \geqslant T_1$ assumed, while the parameter η_2 is given by

$$\eta_2 = \frac{2J_1\big(\frac{2\pi a\Delta r}{R\lambda}\big)}{\frac{2\pi a\Delta r}{R\lambda}}, \tag{F3}$$

which is related to the source size. In Fig. 7, we can see the behavior of η_2 with respect to the source size. For point sources one can approximate $\eta_2 \approx 1$.

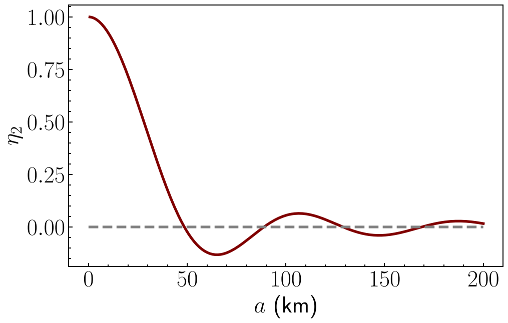

FIG. 7. Plot showing the behavior of η_2 with respect to the radius of the circular disk source with $\Delta r = 2$ m.

1. Quantum Fisher information: Two-point sources

We found the elements of the QFI matrix for estimating the source separation as

$$\begin{aligned}\mathscr{F}_{s_is_j} = {}& \frac{2\pi^2\eta\kappa v_i v_j}{\mathscr{D}_{s_xs_y}}(\eta^2\kappa^2(4T^2-\Delta T^2)\{(4T^2-\Delta T^2)\cos[4\pi(s_xv_x+s_yv_y)]+16T^2\cos[2\pi(s_xv_x+s_yv_y)]\}\\ &-\eta^2\kappa^2(\Delta T^4-24\Delta T^2T^2+80T^4)-128\eta\kappa T^3-32T^2),\end{aligned} \tag{F4}$$

where $i, j = \{x, y\}$ and the denominator is given by

$$\begin{aligned}\mathscr{D}_{s_xs_y} = {}& \eta\kappa(4T^2-\Delta T^2)\{\eta^2\kappa^2(\Delta T^2-4T^2)\cos[4\pi(s_xv_x+s_yv_y)]\\ &+4[\eta\kappa(-\Delta T^2\eta\kappa+4\eta\kappa T^2+6T)+1]\cos[2\pi(s_xv_x+s_yv_y)]\}\\ &-3\eta^3\kappa^3(\Delta T^2-4T^2)^2+24\eta^2\kappa^2T(\Delta T^2-4T^2)+4\eta\kappa(\Delta T^2-20T^2)-16T.\end{aligned} \tag{F5}$$

The elements of QFI matrix for estimating the centroid becomes

$$\mathscr{F}_{t_it_j} = \frac{16\pi^2 v_i v_j\eta\kappa}{\mathscr{D}_t}[(4T^2-\Delta T^2)\cos(2\pi(s_xv_x+s_yv_y))+\Delta T^2+4T^2], \tag{F6}$$

where the denominator is

$$\mathscr{D}_t = 4T+4\eta\kappa T^2-\Delta T^2\eta\kappa-\eta\kappa(4T^2-\Delta T^2)\cos[2\pi(s_xv_x+s_yv_y)]. \tag{F7}$$

Off-diagonal elements of the QFI matrix can be found as

$$\mathscr{F}_{s_it_j} = \frac{32\pi^2\Delta T\eta\kappa T v_i v_j}{\Delta T^2\eta\kappa+\eta\kappa(4T^2-\Delta T^2)\cos[2\pi(s_xv_x+s_yv_y)]-4\eta\kappa T^2-4T}. \tag{F8}$$

If we align two antennas parallel to the source separation, $v_x \to v$ and $v_y \to 0$. In the limit where $\Delta T \to 0$ the QFI for the source separation simplifies to

$$\mathscr{F}_s \to \frac{4\pi^2 v^2\eta\kappa T[\eta\kappa T\ \cos(2\pi sv)+3\eta\kappa T+1]}{[1+4\eta\kappa T+2\eta^2\kappa^2T^2-2\eta^2\kappa^2T^2\cos(2\pi sv)]}, \tag{F9}$$

and the QFI for the centroid simplifies to

$$\mathscr{F}_t \to \frac{32\pi^2v^2\eta\kappa T\ \cos^2(\pi sv)}{1+\eta\kappa T-\eta\kappa T\ \cos(2\pi sv)}, \tag{F10}$$

which agrees with the results in Ref. [35] for $(\Delta T = 0, v_y = 0, s_y = 0, t_y = 0)$ as expected.

2. Elements of the matrix $\mathbf{M}_i$ for a two-mode interferometer: Two-point sources

For simplicity let us assume that $\Delta T \to 0$. Then we have the elements of the matrix $\mathbf{M}_i$ for a two-mode interferometer for estimating the source sizes as

$$\begin{aligned}g^1_{s_i} &= \frac{\pi v_i(4\eta\kappa T+1)\cot[\pi(s_xv_x+s_yv_y)]}{\{1+4\eta\kappa T+2\eta^2\kappa^2T^2-2\eta^2\kappa^2T^2\cos[2\pi(s_xv_x+s_yv_y)]\}},\\ g^2_{s_i} &= \frac{\pi v_i\{\eta\kappa T\cos[2\pi(s_xv_x+s_yv_y)]+3\eta\kappa T+1\}\csc[\pi(s_xv_x+s_yv_y)]\exp(-i\delta_s)}{\{1+4\eta\kappa T+2\eta^2\kappa^2T^2-2\eta^2\kappa^2T^2\cos[2\pi(s_xv_x+s_yv_y)]\}},\end{aligned} \tag{F11}$$

and

$$\begin{aligned}g^1_{t_i} &= 0,\\ g^2_{t_i} &= \frac{2\pi v\cos[\pi(s_xv_x+s_yv_y)]\exp(-i\delta_t)}{1+\eta\kappa T-\eta\kappa T\ \cos[2\pi(s_xv_x+s_yv_y)]},\end{aligned} \tag{F12}$$

where $\delta_s = 2\pi(t_xv_x+t_yv_y)-\pi$ and $\delta_t = 2\pi(t_xv_x+t_yv_y)+\pi/2$.

3. Classical Fisher information for heterodyne detection: Two-point sources

Using the CFI given for the heterodyne detection in Eq. (D3), and assuming that both sources have the same temperature ($\Delta T \to 0$), one can find the CFI for estimating the centroid as

$$F_{t_i} = \frac{32\pi^2\eta^2\kappa^2T^2v_i^2(2\eta\kappa T+1)^2\cos^2[\pi(s_xv_x+s_yv_y)]}{\{-2\eta^2\kappa^2T^2\cos[2\pi(s_xv_x+s_yv_y)]+2\eta\kappa T(\eta\kappa T+2)+1\}^2}. \tag{F13}$$

Again assuming ($\Delta T \to 0$), we can find the CFI for estimating the source separation as

$$\begin{aligned}F_{s_i} = {} & \frac{1}{D_s} 8\pi^2\eta^2\kappa^2T^2 v_i^2 \sin^2[\pi(s_x v_x + s_y v_y)](2\eta\kappa T+1)^2(1 - 14\eta^4\kappa^4T^4\cos[4\pi(s_xv_x+s_yv_y)] \\ & - 4\eta^2\kappa^2T^2\cos[2\pi(s_xv_x+s_yv_y)][2\eta\kappa T(9\eta\kappa T+2)+1] - 2\eta\kappa T\{\eta\kappa T[\eta\kappa T(21\eta\kappa T-8)-10]-4\}),\end{aligned} \tag{F14}$$

where the denominator is given by

$$D_s = \{1 + 4\eta\kappa T + 2\eta^2\kappa^2T^2 - 2\eta^2\kappa^2T^2\cos[2\pi(s_xv_x+s_yv_y)]\}^4. \tag{F15}$$

---

[1] S. W. Hell and J. Wichmann, Breaking the diffraction resolution limit by stimulated emission: Stimulated-emission-depletion fluorescence microscopy, Opt. Lett. **19**, 780 (1994).

[2] S. W. Hell, Far-Field Optical Nanoscopy, Science **316**, 1153 (2007).

[3] M. Tsang, R. Nair, and X.-M. Lu, Quantum Theory of Superresolution for Two Incoherent Optical Point Sources, Phys. Rev. X **6**, 031033 (2016).

[4] C. W. Helstrom, Detection theory and quantum mechanics, Inform. Comput. **10**, 254 (1967).

[5] C. W. Helstrom, Quantum detection and estimation theory, J. Stat. Phys. **1**, 231 (1969).

[6] C. W. Helstrom, Cramer-Rao inequalities for operator-valued measures in quantum mechanics, Int. J. Theor. Phys. **8**, 361 (1973).

[7] C. W. Helstrom, Estimation of Object Parameters by a Quantum-Limited Optical System, J. Opt. Soc. Am. **60**, 233 (1970).

[8] M. Tsang, Quantum limits to optical point-source localization, Optica **2**, 646 (2015).

[9] M. Tsang, Quantum limit to subdiffraction incoherent optical imaging, Phys. Rev. A **99**, 012305 (2019).

[10] S. Zhou and L. Jiang, Modern description of Rayleigh's criterion, Phys. Rev. A **99**, 013808 (2019).

[11] G. Sorelli, M. Gessner, M. Walschaers, and N. Treps, Moment-based superresolution: Formalism and applications Phys. Rev. A **104**, 033515 (2021).

[12] J. Řehaček, Z. Hradil, B. Stoklasa, M. Paúr, J. Grover, A. Krzic, and L. L. Sánchez-Soto, Multiparameter quantum metrology of incoherent point sources: Towards realistic superresolution, Phys. Rev. A **96**, 062107 (2017).

[13] C. Napoli, S. Piano, R. Leach, G. Adesso, and T. Tufarelli, Towards Superresolution Surface Metrology: Quantum Estimation of Angular and Axial Separations, Phys. Rev. Lett. **122**, 140505 (2019).

[14] R. Nair and M. Tsang, Far-Field Superresolution of Thermal Electromagnetic Sources at the Quantum Limit, Phys. Rev. Lett. **117**, 190801 (2016).

[15] C. Lupo and S. Pirandola, Ultimate Precision Bound of Quantum and Subwavelength Imaging, Phys. Rev. Lett. **117**, 190802 (2016).

[16] W. Larson and B. E. A. Saleh, Resurgence of Rayleigh's curse in the presence of partial coherence, Optica **5**, 1382 (2018).

[17] S. Kurdziałek and R. Demkowicz-Dobrzański, Super-resolution optical fluctuation imaging—fundamental estimation theory perspective, J. Opt. **23**, 075701 (2021).

[18] M. I. Kolobov and C. Fabre, Quantum Limits on Optical Resolution, Phys. Rev. Lett. **85**, 3789 (2000).

[19] S. Z. Ang, R. Nair, and M. Tsang, Quantum limit for two-dimensional resolution of two incoherent optical point sources, Phys. Rev. A **95**, 063847 (2017).

[20] E. Bisketzi, D. Branford, and A. Datta, Quantum limits of localisation microscopy, New J. Phys. **21**, 123032 (2019).

[21] M. Bojer, Z. Huang, S. Karl, S. Richter, P. Kok, and J. von Zanthier, A quantitative comparison of amplitude versus intensity interferometry for astronomy, New J. Phys. **24**, 043026 (2022).

[22] C. Datta, M. Jarzyna, Y. L. Len, K. Łukanowski, J. Kołodyński, and K. Banaszek, Sub-Rayleigh resolution of two incoherent sources by array homodyning, Phys. Rev. A **102**, 063526 (2020).

[23] J. O. de Almeida, J. Kołodyński, C. Hirche, M. Lewenstein, and M. Skotiniotis, Discrimination and estimation of incoherent sources under misalignment, Phys. Rev. A **103**, 022406 (2021).

[24] K. Liang, S. A. Wadood, and A. N. Vamivakas, Coherence effects on estimating general sub-rayleigh object distribution moments Phys. Rev. A **104**, 022220 (2021).

[25] M. Tsang, Subdiffraction incoherent optical imaging via spatial-mode demultiplexing, New J. Phys. **19**, 023054 (2017).

[26] O. Pinel, J. Fade, D. Braun, P. Jian, N. Treps, and C. Fabre, Ultimate sensitivity of precision measurements with intense Gaussian quantum light: A multimodal approach, Phys. Rev. A **85**, 010101(R) (2012).

[27] M. P. Backlund, Y. Shechtman, and R. L. Walsworth, Fundamental Precision Bounds for Three-Dimensional Optical Localization Microscopy with Poisson Statistics, Phys. Rev. Lett. **121**, 023904 (2018).

[28] M. Mazelanik, A. Leszczynski, and M. Parniak, Optical-domain spectral super-resolution enabled by a quantum memory, Nat. Commun. **13**, 691 (2022).

[29] M. Paúr, B. Stoklasa, Z. Hradil, L. L. Sánchez-Soto, and J. Rehacek, Achieving the ultimate optical resolution, Optica **3**, 1144 (2016).

[30] A. A. Pushkina, G. Maltese, J. I. Costa-Filho, P. Patel, and A. I. Lvovsky, Super-Resolution Linear Optical Imaging in the Far Field, Phys. Rev. Lett. **127**, 253602 (2021).

[31] C. Lupo, Z. Huang, and P. Kok, Quantum Limits to Incoherent Imaging are Achieved by Linear Interferometry, Phys. Rev. Lett. **124**, 080503 (2020).

[32] D. Gottesman, T. Jennewein, and S. Croke, Longer-Baseline Telescopes Using Quantum Repeaters, Phys. Rev. Lett. **109**, 070503 (2012).

[33] E. T. Khabiboulline, J. Borregaard, K. De Greve, and M. D. Lukin, Optical Interferometry with Quantum Networks, Phys. Rev. Lett. **123**, 070504 (2019).

[34] M. Tsang, Quantum Nonlocality in Weak-Thermal-Light Interferometry, Phys. Rev. Lett. **107**, 270402 (2011).

[35] Y. Wang, Y. Zhang, and V. O. Lorenz, Superresolution in interferometric imaging of strong thermal sources, Phys. Rev. A **104**, 022613 (2021).

[36] E. Anterrieu, A resolving matrix approach for synthetic aperture imaging radiometers, IEEE Trans. Geosci. Remote Sens. **42**, 1649 (2004).

[37] I. Corbella, N. Duffo, M. Vall-llossera, A. Camps, and F. Torres, The visibility function in interferometric aperture synthesis radiometry, IEEE Trans. Geosci. Remote Sens. **42**, 1677 (2004).

[38] D. Le Vine, Synthetic aperture radiometer systems, IEEE Trans. Microw. Theory Tech. **47**, 2228 (1999).

[39] A. R. Thompson, J. M. Moran, and George W. Swenson Jr., *Interferometry and Synthesis in Radio Astronomy* (Springer, Cham, 2017).

[40] P. van Cittert, Die wahrscheinliche schwingungsverteilung in einer von einer lichtquelle direkt oder mittels einer linse beleuchteten ebene, Physica (Amsterdam) **1**, 201 (1934).

[41] F. Zernike, The concept of degree of coherence and its application to optical problems, Physica (Amsterdam) **5**, 785 (1938).

[42] D. Braun, Y. Monjid, B. Rougé, and Y. Kerr, Generalization of the Van Cittert–Zernike theorem: Observers moving with respect to sources, Meas. Sci. Technol. **27**, 015002 (2016).

[43] D. Braun, Y. Monjid, B. Rougé, and Y. Kerr, Fourier-correlation imaging, J. Appl. Phys. **123**, 074502 (2018).

[44] J. R. Jeffers, N. Imoto, and R. Loudon, Quantum optics of traveling-wave attenuators and amplifiers, Phys. Rev. A **47**, 3346 (1993).

[45] J. Liu, H. Yuan, X.-M. Lu, and X. Wang, Quantum Fisher information matrix and multiparameter estimation, J. Phys. A: Math. Theor. **53**, 023001 (2020).

[46] O. Pinel, P. Jian, N. Treps, C. Fabre, and D. Braun, Quantum parameter estimation using general single-mode Gaussian states, Phys. Rev. A **88**, 040102(R) (2013).

[47] J. Shapiro, The Quantum Theory of Optical Communications, IEEE J. Sel. Top. Quantum Electron. **15**, 1547 (2009).

[48] J. S. Sidhu and P. Kok, Geometric perspective on quantum parameter estimation, AVS Quantum Sci. **2**, 014701 (2020).

[49] D. Šafránek, Estimation of Gaussian quantum states, J. Phys. A: Math. Theor. **52**, 035304 (2019).

[50] R. Nichols, P. Liuzzo-Scorpo, P. A. Knott, and G. Adesso, Multiparameter Gaussian quantum metrology, Phys. Rev. A **98**, 012114 (2018).

[51] D. Braun, G. Adesso, F. Benatti, R. Floreanini, U. Marzolino, M. W. Mitchell, and S. Pirandola, Quantum-enhanced measurements without entanglement, Rev. Mod. Phys. **90**, 035006 (2018).

[52] A. Holevo, Statistical decision theory for quantum systems, J. Multivariate Anal. **3**, 337 (1973).

[53] S. Ragy, M. Jarzyna, and R. Demkowicz-Dobrzański, Compatibility in multiparameter quantum metrology, Phys. Rev. A **94**, 052108 (2016).

[54] C. Oh, S. Zhou, Y. Wong, and L. Jiang, Quantum Limits of Superresolution in a Noisy Environment, Phys. Rev. Lett. **126**, 120502 (2021).

[55] M. Gessner, C. Fabre, and N. Treps, Superresolution Limits from Measurement Crosstalk, Phys. Rev. Lett. **125**, 100501 (2020).

[56] Y. L. Len, C. Datta, M. Parniak, and K. Banaszek, Resolution limits of spatial mode demultiplexing with noisy detection, Int. J. Quantum Inf. **18**, 1941015 (2020).

[57] K. J. Blow, R. Loudon, S. J. D. Phoenix, and T. J. Shepherd, Continuum fields in quantum optics, Phys. Rev. A **42**, 4102 (1990).

[58] L. Mandel, E. Wolf, and P. Meystre, Optical Coherence and Quantum Optics, Am. J. Phys. **64**, 1438 (1996).

[59] R. J. Glauber, Coherent and Incoherent States of the Radiation Field, Phys. Rev. **131**, 2766 (1963).

[60] M. O. Scully, M. S. Zubairy, and I. A. Walmsley, Quantum Optics, Am. J. Phys. **67**, 648 (1999).

[61] R. Loudon and T. von Foerster, The Quantum Theory of Light, Am. J. Phys. **42**, 1041 (1974).

[62] J. Zmuidzinas, Cramér–Rao sensitivity limits for astronomical instruments: Implications for interferometer design, J. Opt. Soc. Am. A **20**, 218 (2003).

[63] J. Zmuidzinas, Thermal noise and correlations in photon detection, Appl. Opt. **42**, 4989 (2003).

[64] R. Kubo, The fluctuation-dissipation theorem, Rep. Prog. Phys. **29**, 255 (1966).

[65] S. Savasta, O. Di Stefano, and R. Girlanda, Light quantization for arbitrary scattering systems, Phys. Rev. A **65**, 043801 (2002).

[66] E. A. Sharkov, *Passive Microwave Remote Sensing of the Earth: Physical Foundations* (Springer, Berlin, 2011).

[67] L. D. Landau, E. M. Lifshits, L. P. Pitaevsk, L. D. Landau, and L. D. Landau, *Statistical Physics* (Pergamon, Oxford, 1980), Vols. 5, 9.

[68] R. Carminati and J.-J. Greffet, Near-Field Effects in Spatial Coherence of Thermal Sources, Phys. Rev. Lett. **82**, 1660 (1999).

[69] D. Braun, P. Jian, O. Pinel, and N. Treps, Precision measurements with photon-subtracted or photon-added Gaussian states, Phys. Rev. A **90**, 013821 (2014).

[70] G. Adesso, S. Ragy, and A. R. Lee, Continuous variable quantum information: Gaussian states and beyond, Open Syst. Inf. Dyn. **21**, 1440001 (2014).

[71] Y. Gao and H. Lee, Bounds on quantum multiple-parameter estimation with Gaussian state, Eur. Phys. J. D **68**, 347 (2014).

[72] S. Olivares, Quantum optics in the phase space: A tutorial on Gaussian states, Eur. Phys. J.: Spec. Top. **203**, 3 (2012).

[73] C. Weedbrook, S. Pirandola, R. García-Patrón, N. J. Cerf, T. C. Ralph, J. H. Shapiro, and S. Lloyd, Gaussian quantum information, Rev. Mod. Phys. **84**, 621 (2012).

[74] M. Szczykulska, T. Baumgratz, and A. Datta, Multi-parameter quantum metrology, Adv. Phys.: X **1**, 621 (2016).

[75] M. Tsang, F. Albarelli, and A. Datta, Quantum Semiparametric Estimation, Phys. Rev. X **10**, 031023 (2020).

[76] F. Albarelli, M. Barbieri, M. Genoni, and I. Gianani, A perspective on multiparameter quantum metrology: From theoretical tools to applications in quantum imaging, Phys. Lett. A **384**, 126311 (2020).

[77] S. L. Braunstein and C. M. Caves, Statistical Distance and the Geometry of Quantum States, Phys. Rev. Lett. **72**, 3439 (1994).

[78] M. G. A. Paris, Quantum estimation for quantum technology, Int. J. Quantum Inf. **07**, 125 (2009).

[79] J. W. Goodman, *Statistical Optics* (Wiley, New York, 1985), Vol. 1, p. 567.

[80] M. E. Pearce, E. T. Campbell, and P. Kok, Optimal quantum metrology of distant black bodies, Quantum **1**, 21 (2017).

[81] L. A. Howard, G. G. Gillett, M. E. Pearce, R. A. Abrahao, T. J. Weinhold, P. Kok, and A. G. White, Optimal Imaging of Remote Bodies Using Quantum Detectors, Phys. Rev. Lett. **123**, 143604 (2019).

[82] R. Lescanne, S. Deléglise, E. Albertinale, U. Réglade, T. Capelle, E. Ivanov, T. Jacqmin, Z. Leghtas, and E. Flurin, Irreversible Qubit-Photon Coupling for the Detection of Itinerant Microwave Photons, Phys. Rev. X **10**, 021038 (2020).

[83] C. S. Wang, J. C. Curtis, B. J. Lester, Y. Zhang, Y. Y. Gao, J. Freeze, V. S. Batista, P. H. Vaccaro, I. L. Chuang, L. Frunzio, L. Jiang, S. M. Girvin, and R. J. Schoelkopf, Efficient Multiphoton Sampling of Molecular Vibronic Spectra on a Superconducting Bosonic Processor, Phys. Rev. X **10**, 021060 (2020).